Neuron

Article

Tau aggregates are RNA-protein assemblies that mislocalize multiple nuclear speckle components

Graphical abstract

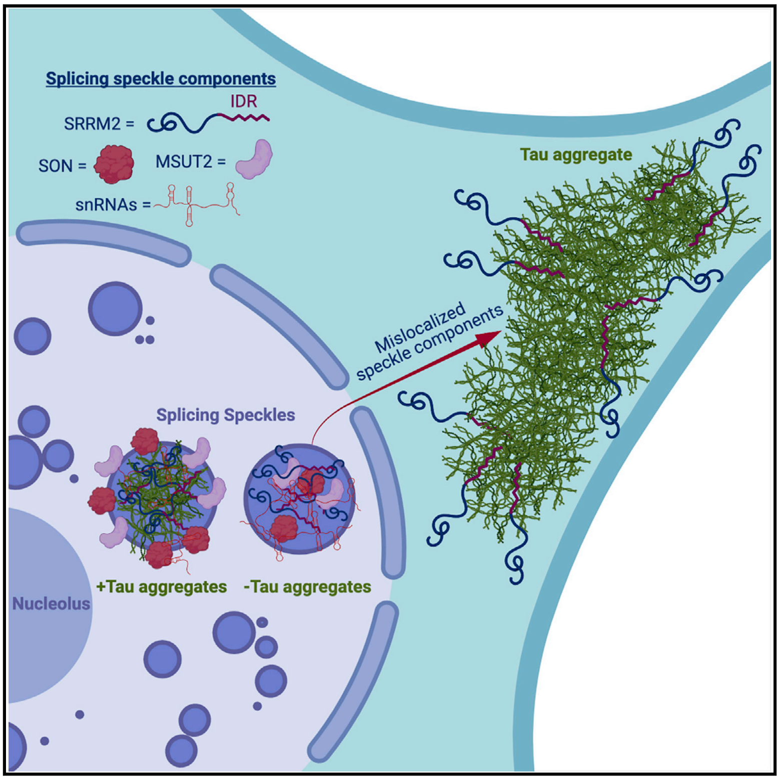

Highlights

- Tau aggregates contain RNA and are enriched for snRNAs and snoRNAs
- Nuclear tau aggregates localize to splicing speckles in model systems
- Tau aggregates alter the composition, organization, and dynamics of speckles
- Speckle components are mislocalized to cytoplasmic tau aggregates in patient brains

Authors

Evan Lester, Felicia K. Ooi,
Nadine Bakkar, ..., George A. Carlson,
Stanley B. Prusiner, Roy Parker

Correspondence

roy.parker@colorado.edu

In brief

Insoluble tau aggregates are present in multiple neurodegenerative diseases, including Alzheimer's disease. In this article, Lester et al. show that tau aggregates are enriched for snRNAs and snoRNAs, alter splicing speckles, and mislocalize nuclear splicing proteins. This could help explain RNA processing defects seen in individuals with tau pathology.

Lester et al., 2021, Neuron *109*, 1–17
May 19, 2021 © 2021 Elsevier Inc.
https://doi.org/10.1016/j.neuron.2021.03.026

CellPress

Please cite this article in press as: Lester et al., Tau aggregates are RNA-protein assemblies that mislocalize multiple nuclear speckle components, Neuron (2021), https://doi.org/10.1016/j.neuron.2021.03.026

Neuron

CellPress

Article

Tau aggregates are RNA-protein assemblies that mislocalize multiple nuclear speckle components

Evan Lester,[1,2] Felicia K. Ooi,[3] Nadine Bakkar,[4] Jacob Ayers,[3,5] Amanda L. Woerman,[6] Joshua Wheeler,[1,2,7] Robert Bowser,[4] George A. Carlson,[3,5] Stanley B. Prusiner,[3,5,8] and Roy Parker[1,9,10,*]

[1]Department of Biochemistry, University of Colorado, Boulder, CO, USA
[2]Medical Scientist Training Program, University of Colorado Anschutz Medical Campus, Aurora, CO, USA
[3]Institute for Neurodegenerative Diseases, Weill Institute for Neurosciences, University of California San Francisco, San Francisco, CA, USA
[4]Department of Neurobiology, Barrow Neurological Institute, Phoenix, AZ, USA
[5]Department of Neurology, Weill Institute for Neurosciences, University of California San Francisco, San Francisco, CA, USA
[6]Department of Biology and Institute for Applied Life Sciences, University of Massachusetts Amherst, Amherst, MA, USA
[7]Department of Pathology, Stanford University, Stanford, CA, USA
[8]Department of Biochemistry and Biophysics, University of California San Francisco, San Francisco, CA, USA
[9]Howard Hughes Medical Institute, University of Colorado, Boulder, CO, USA
[10]Lead contact
*Correspondence: roy.parker@colorado.edu

https://doi.org/10.1016/j.neuron.2021.03.026

SUMMARY

Tau aggregates contribute to neurodegenerative diseases, including frontotemporal dementia and Alzheimer's disease (AD). Although RNA promotes tau aggregation *in vitro*, whether tau aggregates in cells contain RNA is unknown. We demonstrate, in cell culture and mouse brains, that cytosolic and nuclear tau aggregates contain RNA with enrichment for small nuclear RNAs (snRNAs) and small nucleolar RNAs (snoRNAs). Nuclear tau aggregates colocalize with and alter the composition, dynamics, and organization of nuclear speckles, membraneless organelles involved in pre-mRNA splicing. Moreover, several nuclear speckle components, including SRRM2, mislocalize to cytosolic tau aggregates in cells, mouse brains, and brains of individuals with AD, frontotemporal dementia (FTD), and corticobasal degeneration (CBD). Consistent with these alterations, we observe that the presence of tau aggregates is sufficient to alter pre-mRNA splicing. This work identifies tau alteration of nuclear speckles as a feature of tau aggregation that may contribute to the pathology of tau aggregates.

INTRODUCTION

Fibrillar aggregates of the microtubule-associated protein tau (tau) are seen in numerous neurodegenerative diseases collectively referred to as tauopathies (Orr et al., 2017). Tauopathies have a variety of etiologies ranging from mutations in tau that promote its aggregation, such as in inherited frontotemporal dementia with parkinsonism-17 (FTDP-17), to environmental triggers, such as head trauma giving rise to chronic traumatic encephalopathy (CTE), to the incompletely understood link between β-amyloid and tauopathy in Alzheimer's disease (AD) (Aoyagi et al., 2019; Goedert et al., 1988; Wischik et al., 1988).

Several lines of evidence suggest that formation and propagation of tau oligomers or aggregates is a key driver of toxicity in tauopathies. First, mutations that promote tau aggregation are causative in FTDP-17 (Goedert and Spillantini, 2000). Second, the rate of cognitive decline in AD is closely related to the rate of tau aggregate formation (Hanseeuw et al., 2019). Third, tau aggregates and tauopathy can be transmitted by inoculation of cells and mice (Aoyagi et al., 2019; Kaufman et al., 2016; Sanders et al., 2014; Woerman et al., 2016). Induction of tau aggregates in cell models can also be toxic (Sanders et al., 2014). Fourth, reduction of tau is neuroprotective in mouse models of AD (DeVos et al., 2018). Understanding how tau oligomers or aggregates form and how they induce neurotoxicity may lead to development of therapeutic agents for numerous neurodegenerative diseases.

Tau is present in the human central nervous system as six splice isoforms. These isoforms differ in the number of N-terminal inserts—0N, 1N, or 2N—and the number of microtubule binding repeat domains (RDs)—3R or 4R (Buée et al., 2000; Park et al., 2016). The N-terminal inserts have been shown to affect tau's localization, interactions with membranes, spacing between microtubules, and signal transduction (Brandt et al., 1995; Chen et al., 1992; Lee et al., 1998; Liu and Götz, 2013). The positively charged RD has been shown to form the core of the amyloid fibrils present in the brains of individuals with tauopathies, and this is also where the majority of disease-causing mutations are found (Buée et al., 2000; Falcon et al., 2018, 2019; Fitzpatrick et al., 2017; Goedert, 2005; Wegmann et al., 2013; Zhang et al., 2020).

Please cite this article in press as: Lester et al., Tau aggregates are RNA-protein assemblies that mislocalize multiple nuclear speckle components, Neuron (2021), https://doi.org/10.1016/j.neuron.2021.03.026

Several observations suggest that RNA may affect formation of tau aggregates. First, tau binds RNA (Dinkel et al., 2015; Schröder et al., 1984; Wang et al., 2006; Zhang et al., 2017). Second, *in vitro* RNA promotes conversion of soluble tau into insoluble aggregated tau, possibly because the negatively charged phosphate backbone of RNA can neutralize the positively charged RD of tau, allowing tighter packing of tau molecules and cross-β fibril formation (Ambadipudi et al., 2017; Dinkel et al., 2015; Kampers et al., 1996). Third, tau immunopurifies with a number of RNA binding proteins in the aggregated and unaggregated states (Bai et al., 2013; Broccolini et al., 2000; Gunawardana et al., 2015; Hales et al., 2014a, 2014b; Hsieh et al., 2019; Meier et al., 2016). Fourth, tau aggregates in AD and Pick's disease have been found to stain positive for RNA using RNA dyes (Ginsberg et al., 1997, 1998). Finally, analysis of the RNAs interacting with tau in an unaggregated state by iCLIP (individual-nucleotide resolution cross-linking and immunoprecipitation) suggests that tau interacts preferentially with tRNAs (Zhang et al., 2017). Thus, an important question is whether pathological tau aggregates contain RNA, and if so, what is the nature of that RNA and the possible physiologic or pathologic consequences of their interaction.

Here we investigated the RNA composition of tau aggregates in cell culture and mouse model systems. Similar to earlier results, we found that tau aggregates form in the cytosol and the nucleus (Bukar Maina et al., 2016; Gil et al., 2017; Brady et al., 1995; Sanders et al., 2014; Ulrich et al., 2018). We found that cytosolic and nuclear tau aggregates contain RNA and are enriched for RNAs involved in RNA splicing and modification, including small nuclear RNAs (snRNAs) and small nucleolar RNAs (snoRNAs), as well as repetitive Alu RNAs. We also found that nuclear tau aggregates contain snRNAs and are concentrated in and alter the composition, organization, and dynamics of nuclear speckles, non-membranous assemblies of RNA and protein containing nascent RNA transcripts and splicing machinery (also known as splicing speckles or just speckles) (Galganski et al., 2017). Surprisingly, we discovered that serine arginine repetitive matrix protein 2 (SRRM2), a protein component of splicing speckles, mislocalizes from nuclear splicing speckles to cytosolic tau aggregates in cellular models of tauopathy, tauopathy mouse models, and individuals with AD, frontotemporal lobar degeneration (FTLD), and corticobasal degeneration (CBD). These extensive interactions of tau with splicing speckles and splicing machinery correlate with splicing alterations seen in cells that form tau aggregates. This is notably similar to how cytosolic sequestration of RNA binding proteins, such as TDP-43 and FUS in amyotrophic lateral sclerosis (ALS), can lead to alterations in nuclear RNA processing, promoting neurodegeneration (Lagier-Tourenne et al., 2012; Polymenidou et al., 2011).

RESULTS

Cytosolic and nuclear tau aggregates contain RNA

To determine whether tau aggregates contain RNA, we employed a previously developed HEK293 tau biosensor cell line (Holmes et al., 2014; Sanders et al., 2014). The HEK293 biosensor cells express the 4R repeat domain (RD) of tau, with the P301S mutation tagged with cyan fluorescent protein (CFP) or yellow fluorescent protein (YFP). Fluorescent tau aggregates can be induced in these HEK293 cells via lipofection of preformed non-fluorescent tau aggregates isolated from the brains of mice expressing 0N4R tau with the P301S mutation (P301S mice, Tg2541) (Holmes et al., 2014; Sanders et al., 2014). As seen previously (Sanders et al., 2014), we observed fluorescent tau aggregates in the cytosol and nucleus of the HEK293 cells following transfection of clarified brain homogenate from mice expressing P301S human tau but not from mice expressing wild-type (WT) tau (WT mice, Tg21221), which do not develop tauopathy (Figures 1A and 1B). Nuclear tau aggregates are not an artifact of the truncated K18 tau expressed in HEK293 cells because we also observed formation of nuclear and cytosolic tau aggregates in a tau seeding model expressing full-length P301S 0N4R tau-YFP in H4 neuroglioma cells (Figure S1A; Video S2). Consistent with these fluorescent bodies being insoluble tau aggregates, fluorescence recovery after photobleaching (FRAP) revealed that nuclear and cytosolic tau aggregates are immobile and do not recover after photobleaching (Figures S1B and S1C).

Using fluorescence *in situ* hybridization (FISH) for poly(A) RNA, we observed that cytosolic and nuclear tau aggregates showed 1.5- and 1.72-fold enrichment of poly(A)$^+$ RNA staining, respectively (Figure S1D). We also examined the presence of poly(A) RNA in tau aggregates in the brains of 6-month-old P301S mice, in which transmissible tau aggregates start to form at 1.5 months (Holmes et al., 2014; Yoshiyama et al., 2007). Unlike in humans, where tau pathology develops in the frontal cortex, tau pathology in P301S mice develops primarily in the hindbrain (Johnson et al., 2017). Nuclear tau and tau aggregates have been observed previously in the brains of mice and humans; however, their function and role in disease are poorly understood (Bengoa-Vergniory et al., 2021; Bukar Maina et al., 2016; Gil et al., 2017; Jiang et al., 2019; Liu and Götz, 2013; Metuzals et al., 1988; Montalbano et al., 2020; Papasozomenos, 1995; Brady et al., 1995; Ulrich et al., 2018). We observed that nuclear tau aggregates in the hindbrain stain strongly for poly(A) RNA (Figures 1C, S1E, and S7A; Video S1). We also observed redistribution of the poly(A) signal to overlap with the cytosolic tau aggregates in P301S mouse brains (Figures 1C, S1E, and S7A). Thus, in mouse and cellular models of tau pathologies, tau forms cytosolic tangles and nuclear puncta that contain RNA.

Tau aggregates in HEK293 cells and mouse brains are enriched for snRNAs and snoRNAs

To determine the identity of the RNAs present in tau aggregates, we first purified tau aggregates from HEK293 tau biosensor cells using differential centrifugation and fluorescence-activated particle sorting (FAPS) and then sequenced the associated RNA. By comparing the abundance of RNAs in total RNA and tau aggregates, we observed that tau aggregates contain a diverse transcriptome (Figure 2A) and were enriched for small non-coding RNAs, particularly snoRNAs and minor snRNAs (Figure 2B). Some mRNAs were also enriched in tau aggregates, notably mRNAs coding for the voltage-gated calcium channel complex, histone proteins, centrosomal proteins, and proteins involved in splicing regulation (Figures S2A and S2B).

Analysis of RNAs expressed from multicopy genes using RepEnrich (Criscione et al., 2014) showed enrichment of RNAs from multicopy snoRNAs (U3, U17, and U8) and multicopy

Please cite this article in press as: Lester et al., Tau aggregates are RNA-protein assemblies that mislocalize multiple nuclear speckle components, Neuron (2021), https://doi.org/10.1016/j.neuron.2021.03.026

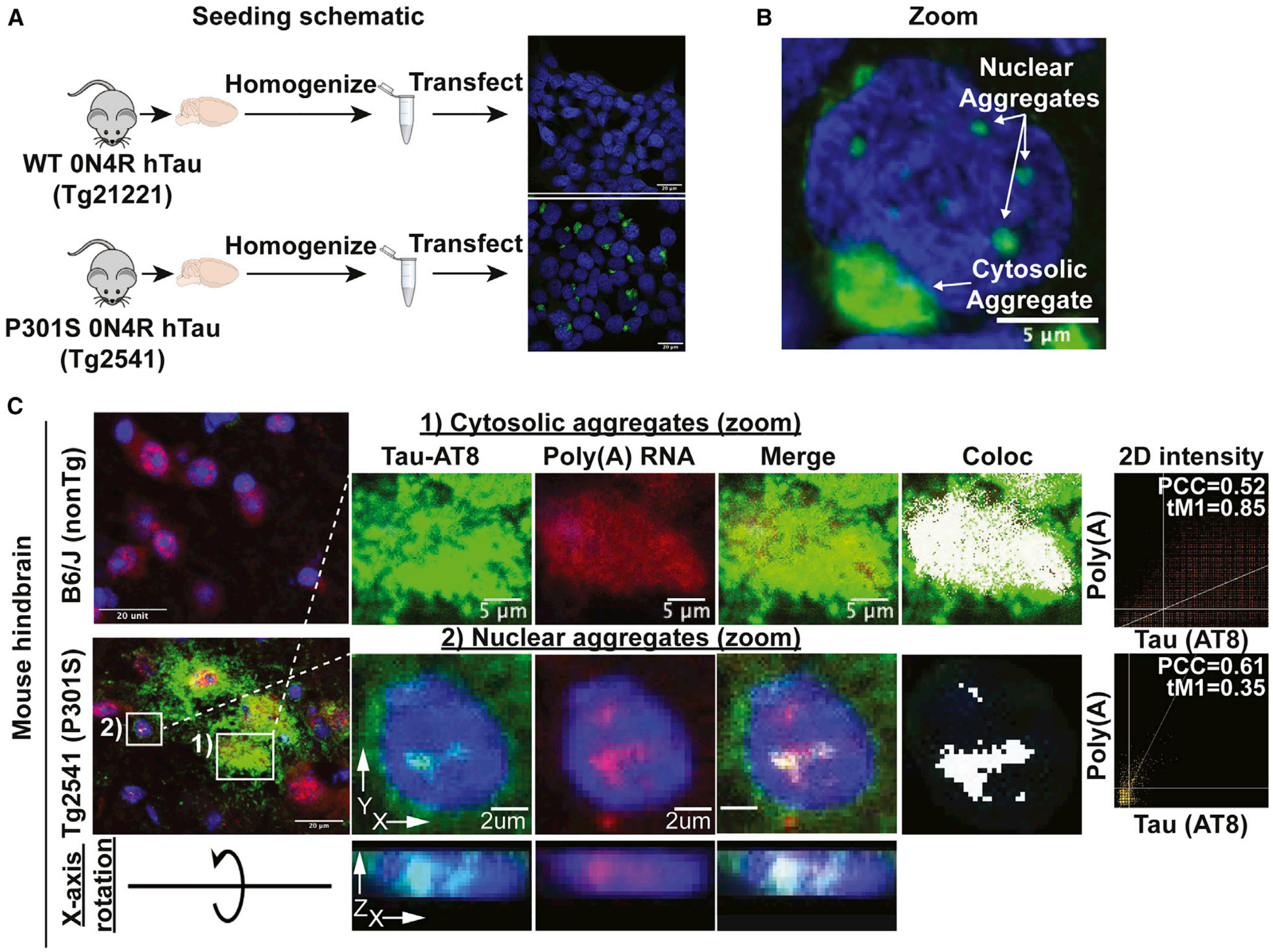

Figure 1. Tau biosensor cell schematic; tau aggregates in mice contain poly(A) RNA

(A) Schematic showing experimental design of tau seeding in HEK293 biosensor cells. Brain homogenate from mice expressing WT (rTg21221) or P301S (rTg2541) 0N4R tau was homogenized, clarified by successive centrifugation, and transfected into HEK293 cells expressing tau K18 (4R repeat domain) tagged with CFP or YFP. Only cells transfected with P301S homogenate formed bright fluorescent aggregates.

(B) Tau aggregates form in the nucleus and cytosol following transfection of P301S tau homogenate.

(C) Cytosolic and nuclear tau aggregates contain poly(A) RNA in the mouse brain. White pixels in the Coloc image show pixels above the Costes determined thresholds in 2D intensity plots (PCC, Pearson correlation coefficient; tM1, thresholded Manders' colocalization [percentage of tau pixels above the threshold that colocalize with poly(A) pixels above the threshold]). The x axis rotation shows AT8 and oligo(dT) staining in the nucleus of mouse Tg2541 cells.

See also Figure S1.

snRNAs (U2 and U1) (Figures S2C and S2D). Consistent with this observation, U1 snRNA has been observed previously to be enriched by PCR in AD tau aggregates (Hales et al., 2014a). Additionally, this analysis showed some enrichment of tRNAs, as observed previously with non-aggregated tau (Zhang et al., 2017). We also observed enrichment of RNAs from specific types of transposable elements; namely, Alu elements (Figures S2C and S2D).

Tau aggregates in P301L mouse brain are also enriched for snRNAs

To investigate whether tau aggregates in mouse brains contain similar RNAs as tau aggregates identified in HEK293 cells, we fractionated mouse brains with 1% sarkosyl extraction followed by tau immunoprecipitation (IP) using the tau-12 antibody to isolate tau aggregates, as described previously (Diner et al., 2017). Western blot analysis showed that sarkosyl extraction enriched for insoluble tau in P301L mice (rTg4510) but not in WT mice (rTg21221) (Figure S2H). To identify RNAs specifically enriched in the aggregated tau fraction, we compared enrichment of RNAs in insoluble tau-12 IP relative to total RNAs between WT and P301L mice (Figure 2C).

Analysis of RNAs enriched in tau aggregates isolated from mouse brains relative to total RNA revealed enrichment of specific RNAs, including snRNAs and snoRNAs, in the P301L tau IP samples (Figures 2C and 2D). This is similar to the RNA composition of tau aggregates isolated from HEK293 cells (Figure S2F). For example, we observed that snoRD115, snoRD104,

Please cite this article in press as: Lester et al., Tau aggregates are RNA-protein assemblies that mislocalize multiple nuclear speckle components, Neuron (2021), https://doi.org/10.1016/j.neuron.2021.03.026

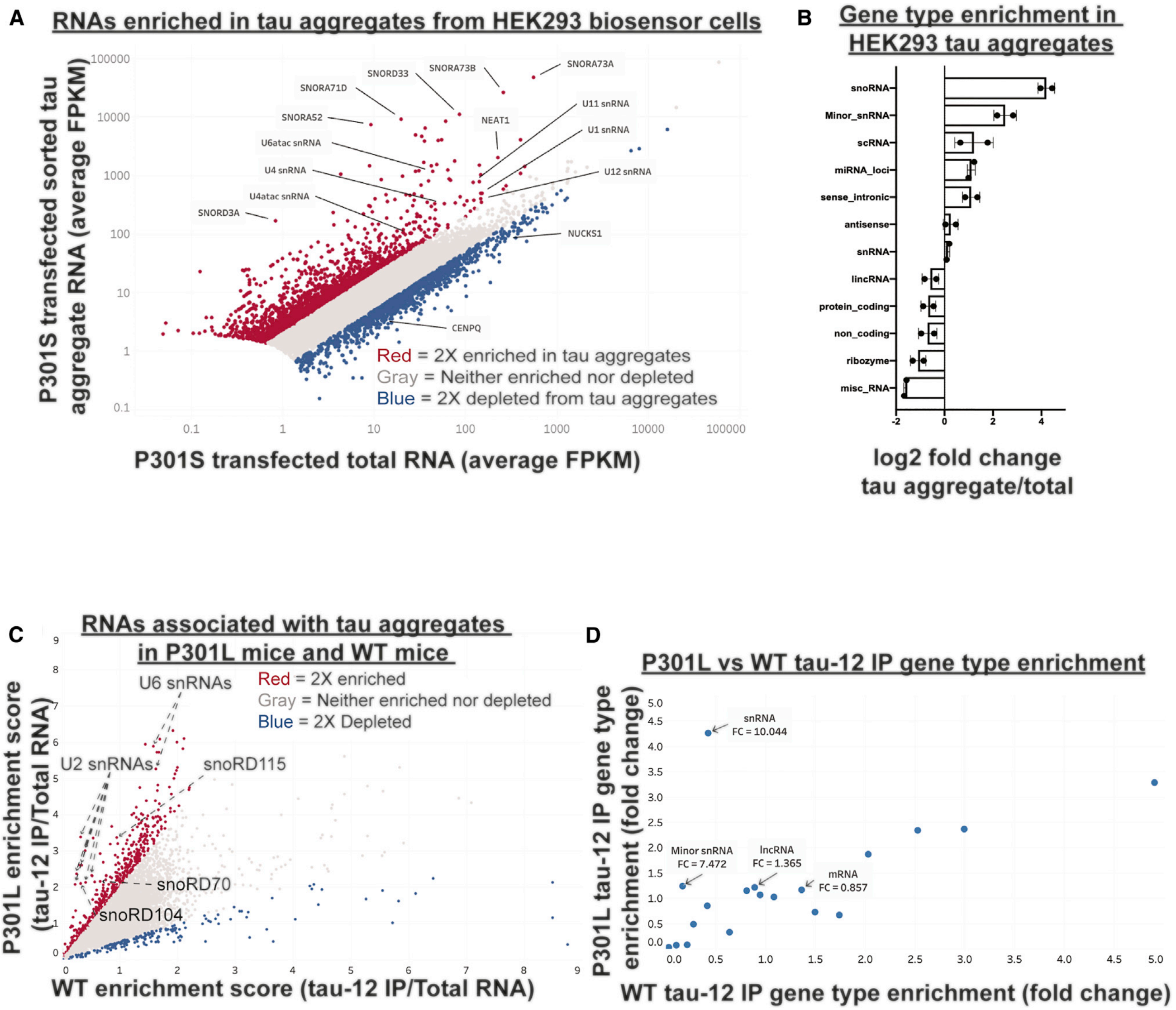

Figure 2. The RNA composition of tau aggregates in cellular and mouse tauopathy model systems

(A) Scatterplot of RNA-seq, showing the average fragments per kilobase per million reads (FPKM) of two replicates for tau aggregate-associated RNA and total RNA. Genes in red are enriched 2-fold in tau aggregates, and genes in blue are depleted 2-fold from tau aggregates. Genes with fewer than 5 FPKM were removed from the analysis because of low coverage.

(B) Fold change in the percentage of total FPKM for each gene type between tau aggregate RNA and total RNA. The percentage of total FPKM was calculated by grouping genes using the Ensembl GRCh38.p13 Biomart gene types.

(C) Scatterplot of RNA-seq data from two replicates of mouse brain tau aggregate isolation in P301L and WT mice. Enrichment scores were calculated by dividing the insoluble tau IP FPKM by the total RNA FPKM for each replicate. Genes in red are enriched 2-fold and genes in blue are depleted 2-fold from P301L sarkosyl-insoluble tau aggregates.

(D) Gene type enrichment in P301L and WT samples. The fold change for each gene type was calculated by dividing the percentage of total FPKM made up by each gene type in the insoluble tau IP by the percentage of total FPKM made up by each gene type in the total RNA. The numbers below the gene type names indicate P301L/WT enrichment.

See also Figure S2.

snoRD70, U2 snRNA, and U6 snRNA were enriched in the P301L insoluble tau fraction (Figure 2C). In contrast to HEK293 tau aggregates, only particular snoRNAs were enriched. This could be due to a variety of factors, including differences in the isoforms of tau expressed in the two models (the RD of tau in HEK293 cells versus full-length 0N4R tau in rTg4510 mice), the mutation in tau itself (P301S in HEK293 biosensor cells and P301L in rTg4510 mice), or differences in the RNA expression profiles of HEK293 cells and mouse neurons. The sarkosyl-insoluble fractions from P301L and WT mice revealed little to no enrichment of snRNAs or minor snRNAs, suggesting that RNAs enriched in tau-12 IP interact with aggregated tau rather than just being enriched in

Please cite this article in press as: Lester et al., Tau aggregates are RNA-protein assemblies that mislocalize multiple nuclear speckle components, Neuron (2021), https://doi.org/10.1016/j.neuron.2021.03.026

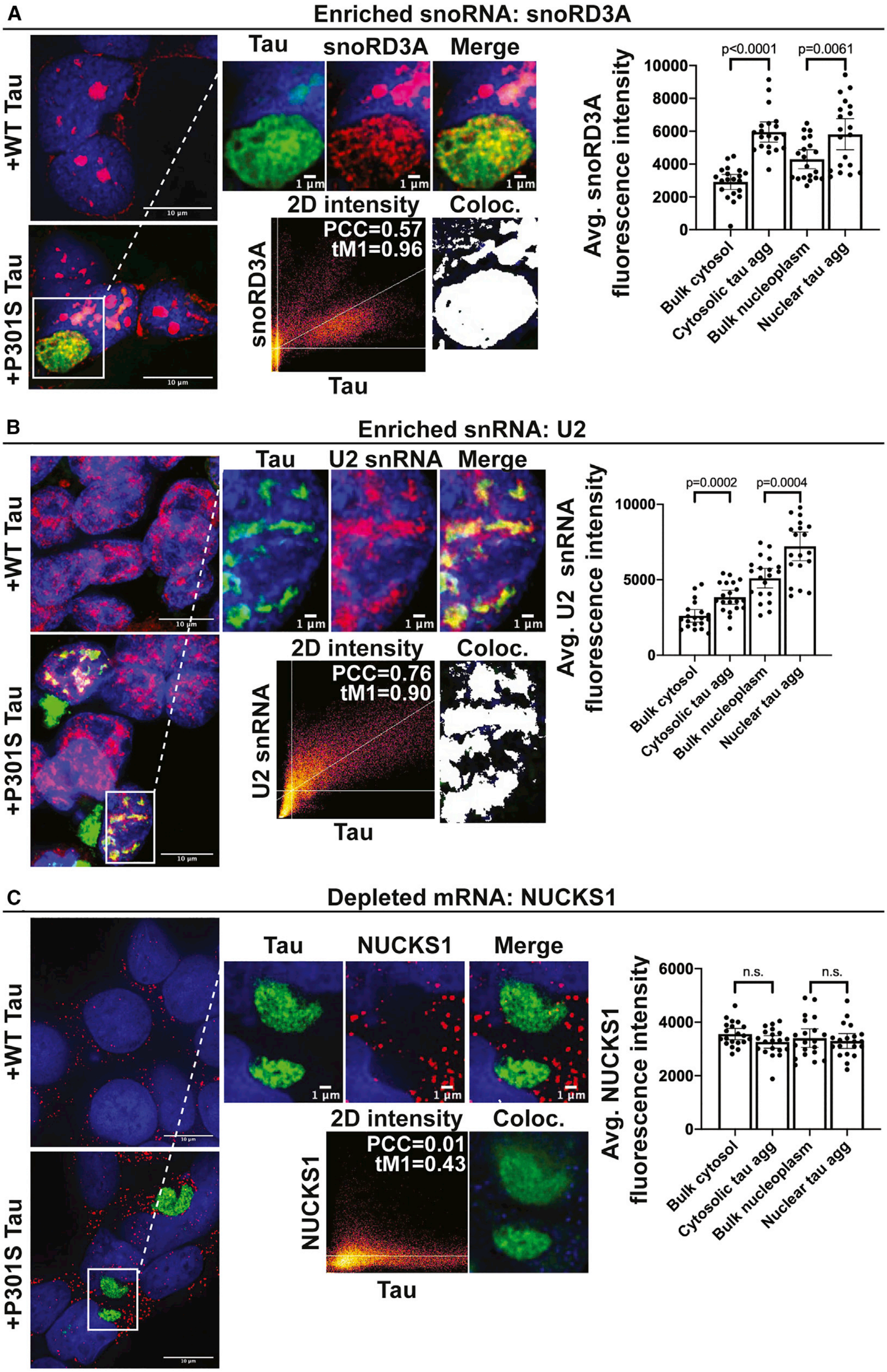

(legend on next page)

the insoluble fraction (Figure S2E). Similar to HEK293 cells, we observed some mRNAs to be enriched in tau aggregates from mouse brains (Figure S2G). Interestingly, some of the most enriched mRNAs are components of the centrosome (PCNT, Cep250, Cep164, and Cep131) (Delaval and Doxsey, 2010; Graser et al., 2007), which is in agreement with previous work that has shown cytosolic tau aggregates concentrating at the centrosomes (Sanders et al., 2014; Santa-Maria et al., 2012). mRNAs coding for centrosomal proteins, such as PCNT, have been described previously to be present at the centrosome, where they are translated locally and could become ensnared in tau aggregates (Sepulveda et al., 2018). Our results demonstrate that isolated pathological tau aggregates in mouse brains are enriched for similar types of RNAs as tau aggregates in HEK293 cells, including snRNAs and snoRNAs.

Enriched RNAs localize to tau aggregates by FISH

We used FISH to examine whether RNA enriched in tau aggregates identified by RNA sequencing localized to cytosolic and/or nuclear tau aggregates. We performed FISH for two enriched snRNAs (U2 and RNU6ATAC), two enriched snoRNAs (snoRA73B and snoRD3A), two depleted mRNAs (CENPQ and NUCKS1), and the enriched Alu family of multicopy RNAs (Figures 3 and S3). Interestingly, we observed that enrichment of specific RNAs differed with respect to the localization of tau aggregates. Specifically, snoRD3A had a 2.05-fold enrichment into cytosolic tau aggregates relative to bulk cytosol, whereas nuclear tau aggregates had a 1.35-fold enrichment of snoRD3A relative to bulk nucleoplasm (Figure 3A). For U2 snRNA, cytosolic and nuclear tau aggregates had roughly the same fold enrichment over their respective compartments (1.48 and 1.42), but the absolute intensity of U2 snRNA in nuclear tau aggregates was 1.87-fold higher than that of cytosolic tau aggregates (Figure 3B). In cells without tau aggregates, U2 snRNA localizes into discrete nuclear foci called splicing speckles, non-membranous RNA-protein assemblies containing factors involved in mRNA splicing (Kota et al., 2008; Wagner et al., 2004; Zhang et al., 2016). Nuclear colocalization of splicing speckle-associated snRNAs with tau implies that nuclear tau aggregation occurs in nuclear speckles (see below). Consistent with this observation, we also see colocalization of the enriched RNU6ATAC snRNA in nuclear tau aggregates (Figure S3A).

We also performed FISH for an Alu consensus sequence present in the Alu RNAs enriched from the sequencing data (Figures S2C and S2D) and found that the Alu signal enriched into both nuclear and cytosolic tau aggregates (Figure S3C). Alu enrichment was greater in cytosolic aggregates (1.56-fold, $p < 0.0001$) than in nuclear aggregates (1.23-fold, $p = 0.02$). In nuclear aggregates, Alu intensity was greatest on the periphery of aggregates. The depleted mRNA NUCKS1 did not show significant intensity enrichment into nuclear or cytosolic tau aggregates (Figure 3C). Similarly, no positive localization correlation could be found for the depleted mRNA CENPQ and tau (Figure S3D). Thus, tau aggregates contain and are enriched for a diverse set of specific RNAs.

Nuclear tau aggregates colocalize with nuclear speckles in HEK293 cells

Because of the bias in the HEK293 and mouse tau aggregate transcriptomes toward nuclear snRNAs and snoRNAs, we explored whether nuclear tau aggregates localized to the nucleolus, where snoRNAs are concentrated, or nuclear speckles, which are enriched in snRNAs (Spector and Lamond, 2011).

Three lines of evidence suggest that nuclear tau aggregates colocalize with nuclear speckles. First, a canonical nuclear speckle marker, Abcam antibody ab11826, co-localized with nuclear tau aggregates by immunofluorescence (IF). In IF, the ab11826 antibody recognizes the nuclear speckle protein SRRM2 (Ilik et al., 2020), and in agreement with this specificity, an SRRM2-halo fusion protein also localizes to nuclear tau aggregates and colocalizes with ab11826 (Figures 4A, S4A, and S4B). Similarly, other components of nuclear speckles colocalize with nuclear tau aggregates (see below). Second, nuclear tau aggregates are enriched for poly(A) RNA (Figures 1C, S1D, and S1E; Video S1) and nuclear speckle-associated RNAs, including U2 snRNA (Figures 3B and S2C; Huang et al., 1994). Third, consistent with tau accumulating in nuclear speckles and not with other nuclear RNA foci, nuclear tau aggregates do not colocalize with the nucleolar marker fibrillarin (Kiss, 2002; Figure S4C). In the brains of P301S (Tg2541) mice, we also observe the pTau(S422) signal colocalizing with both SRRM2 and poly(A) in the nucleus (Figure S7A). Thus, nuclear tau aggregates localize to SRRM2-positive nuclear speckles in cell and mouse models of tauopathy.

Multiple nuclear speckle components re-localize to cytoplasmic Tau aggregates

While examining the co-localization of tau and SRRM2 in nuclear speckles in HEK293 cells, we observed that 77% of cytosolic tau aggregates also contained SRRM2, which relocalized to the cytosol (Figures 4A and S4D). Colocalization of nuclear tau aggregates in nuclear speckles and relocalization of SRRM2 to cytosolic tau aggregates were independent of the lipofectamine used to transfect tau into the cell models (Figure S4E).

The accumulation of SRRM2 into cytosolic phospho-tau aggregates was sufficient to deplete nuclear SRRM2 in HEK293 cells and an H4 neuroglioma cell line expressing a full-length 0N4R P301S tau-YFP that forms fewer nuclear tau aggregates (Figures 4C and 4F). Interestingly, in H4 cells that accumulated SRRM2 in cytosolic tau aggregates, nuclear speckles formed with no change in the intensity of the SON protein, a nuclear speckle protein that does not accumulate in cytosolic tau

Figure 3. FISH for RNAs identified by sequencing

(A–C) Line intensity plots and intensity quantification show enrichment of snoRD3A (A) and U2 snRNA (B) in the nucleus and cytosol of HEK293 tau biosensor cells. We observed no enrichment of the depleted mRNA, NUCKS1 (C), into nuclear or cytosolic tau aggregates. Bar graphs show quantification of FISH fluorescence intensity within nuclear and cytosolic tau aggregates in relation to bulk cytosol and nucleoplasm (n = 20 aggregates). Data are represented as mean ± 95% confidence interval. Significance was determined using an unpaired two-tailed t test. White pixels in the Coloc image show pixels above the Costes determined thresholds in 2D intensity plots (tM1, percentage of tau pixels above the threshold that colocalize with red pixels above the threshold). See also Figure S3.

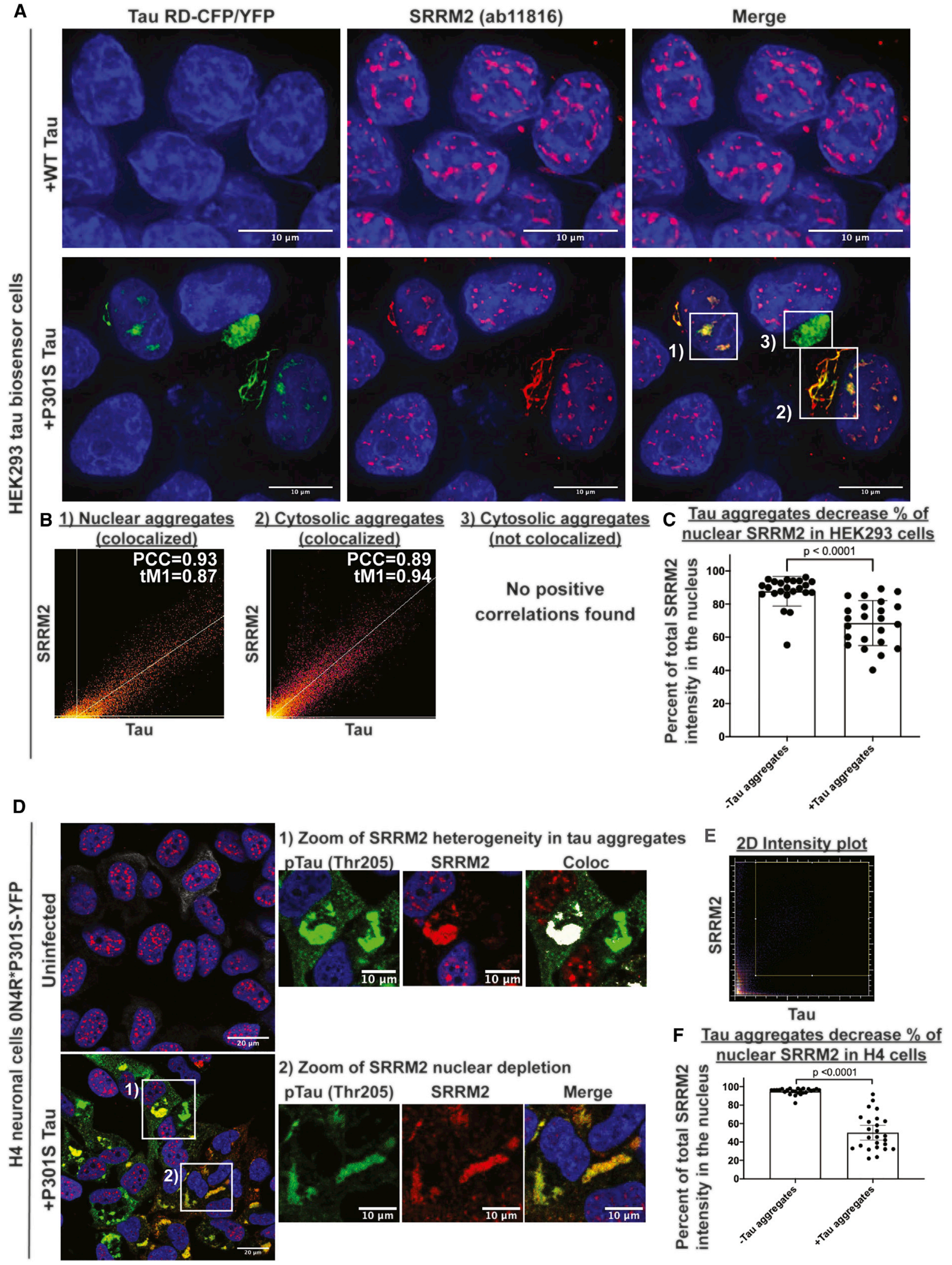

(legend on next page)

aggregates (Figures S4F and S4G). These observations argue that cytosolic tau aggregates deplete the nucleus of SRRM2, which alters the composition of nuclear speckles, but does not prevent formation of nuclear speckles containing SON.

To determine whether other nuclear speckle proteins also re-localized into cytosolic tau aggregates to some extent, we utilized IF to measure the average intensity enrichment of 19 other RNA binding and speckle proteins in nuclear and cytosolic tau aggregates. We observed that the SRRM2 paralogs SRRM1 and SRRM3 did not accumulate in cytosolic tau aggregates (Figure 5A), indicating that this accumulation is not shared between SRRM family members. Similarly, proteins with SR domains did not accumulate in cytosolic tau aggregates (SRSF1, SRSF2, and SRSF3), indicating that an SR domain is not sufficient for accumulation in cytoplasmic tau aggregates (Figure 5A). Some, but not all, nuclear speckle components/splicing factors showed cytosolic tau colocalization, with PNN (a known binding partner of SRRM2), SFPQ, MSUT2, DDX39B, and DYRK1A showing the strongest enrichment scores (Figures 5A and S5A; Zimowska et al., 2003). Thus, multiple nuclear speckle proteins involved in pre-mRNA splicing mislocalize to cytosolic tau aggregates, with SRRM2 and PNN being the most strongly re-localized.

Because neither SR domains nor the N-terminal conserved features of SRRM proteins appeared to be sufficient to recruit proteins to tau aggregates, we hypothesized that the C-terminal domain of SRRM2, which is comprised of an intrinsically disordered region (IDR) (Ilik et al., 2020), might be responsible for SRRM2 recruitment to tau aggregates. This would be consistent with the trend that IDRs of proteins can promote their recruitment to membraneless organelles. To test this idea, we used the CRISPaint system to create two HEK293 tau biosensor cell lines that contained a halo tag inserted into endogenous SRRM2 (Ilik et al., 2020; Schmid-Burgk et al., 2016). These two cell lines were (1) a full-length SRRM2 cell line referred to as SRRM2_FL-halo (insert at amino acid [aa] 2,708) and (2) a cell line lacking the C-terminal IDR of SRRM2, referred to as SRRM2_dIDR-halo (insert at aa 430) (Figures 5C and S5B). We induced tau aggregation in these cells and compared the average SRRM2 halo intensity within nuclear and cytosolic tau aggregates relative to the average intensity in the bulk nucleus or cytosol, respectively.

We observed that SRRM2_FL-halo was recruited to tau aggregates but SRRM2_dIDR-halo was not (Figures 5C–5F). This demonstrated that SRRM2 is recruited to tau aggregates by the disordered C-terminal domain rather than the structured N-terminal domain. Because the N-terminal domain of SRRM2 is sufficient for RNA binding and interactions with the core of the spliceosome (Grainger et al., 2009; Zhang et al., 2018), this result argues that SRRM2 is not recruited to cytosolic tau aggregates by binding RNA nor the core of the spliceosome.

Tau aggregates alter the properties of nuclear speckles, including pre-mRNA splicing

Because cytoplasmic tau aggregates depleted some nuclear speckle components, and tau aggregates can also form in nuclear speckles, we hypothesized that tau aggregate formation might alter the properties and function of nuclear speckles, which we examined in three experiments. First, given that nuclear speckles are highly dynamic structures (Rino et al., 2007), but tau aggregating in speckles was essentially static (Figure S1C), we examined whether nuclear speckles with tau aggregates showed altered dynamics by performing FRAP on two tagged components of speckles, SRRM2 (halo) and SRSF2 (mCherry). We observed that, in the presence of tau aggregates, both nuclear speckle components showed an increase in the static component and a reduced rate of recovery from FRAP (Figures 6A and 6B). This demonstrates that the presence of tau aggregates in nuclear speckles changes their dynamics.

Second, formation of tau aggregates in nuclear speckles alters the organization of speckle components. IF for SRRM2 and SON (a speckle protein that does not relocalize to cytosolic tau aggregates; Figure 5A) showed that the two proteins colocalize in nuclear speckles in the absence of tau aggregates. However, in the presence of nuclear tau aggregates, SRRM2 and tau colocalize in the center of nuclear speckles, whereas SON moves to the periphery and forms a ring-like structure around the aggregate (Figure 6C). MSUT2 displayed a similar redistribution from the center of nuclear speckles to the periphery in the presence of tau aggregates. Interestingly, knockdown of MSUT2 has been shown to suppress tau toxicity in several model systems (Guthrie et al., 2011; Wheeler et al., 2019). These results suggest that formation of tau aggregates in the nucleus disrupts the spatial organization of nuclear speckles.

Third, because nuclear speckles are thought to modulate pre-mRNA splicing (Spector and Lamond, 2011), we performed RNA sequencing (RNA-seq) on the same HEK293 cells with and without tau aggregates to determine whether the presence of tau aggregates could alter splicing. We then investigated splicing patterns using two analyses: MAJIQ and intron retention analysis and detector (iREAD) (Li et al., 2020; Vaquero-Garcia et al., 2016). Using MAJIQ at a ΔPSI threshold of 0.1 and confidence threshold of 0.95, we identified 305 local splicing variations in 226 genes that are differentially spliced (Table S4).

Figure 4. Tau aggregates colocalize with nuclear speckles and mislocalize SRRM2 in cellular tauopathy model systems

(A) Nuclear tau aggregates in HEK293 cells colocalize with SRRM2 (ab11826), a marker of nuclear speckles.

(B) Colocalization analysis showing the relationship between various tau aggregates and SRRM2 (1) nuclear tau aggregates and nuclear speckles marked by SRRM2, (2) a cytosolic tau aggregate that colocalizes with cytosolic SRRM2, and (3) a cytosolic tau aggregate that does not colocalize with SRRM2.

(C) Quantification of the percentage of total SRRM2 intensity in the nucleus in HEK293 cells with and without tau aggregates (n = 23 cells).

(D) IF of phospho-tau (Thr205) and SRRM2 in H4 neuroglioma cells expressing 0N4R*P301S-YFP tau with or without tau aggregates shows that SRRM2 is recruited to 0N4R tau aggregates and recruitment is not dependent on tau phosphorylation at Thr205.

(E) 2D intensity plot for the magnified images showing two Thr205-positive tau aggregates, one that colocalizes with SRRM2 and one that does not colocalize with SRRM2. White pixels in the Coloc image are pixels above the Costes determined thresholds in the 2D intensity plot.

(F) Quantification of the percentage of SRRM2 in the nucleus in cells with and without tau aggregates (n = 25 cells). Images were quantified using CellProfiler. Data are represented as mean ± 95% confidence interval. Significance was determined using an unpaired two-tailed t test.

See also Figure S4.

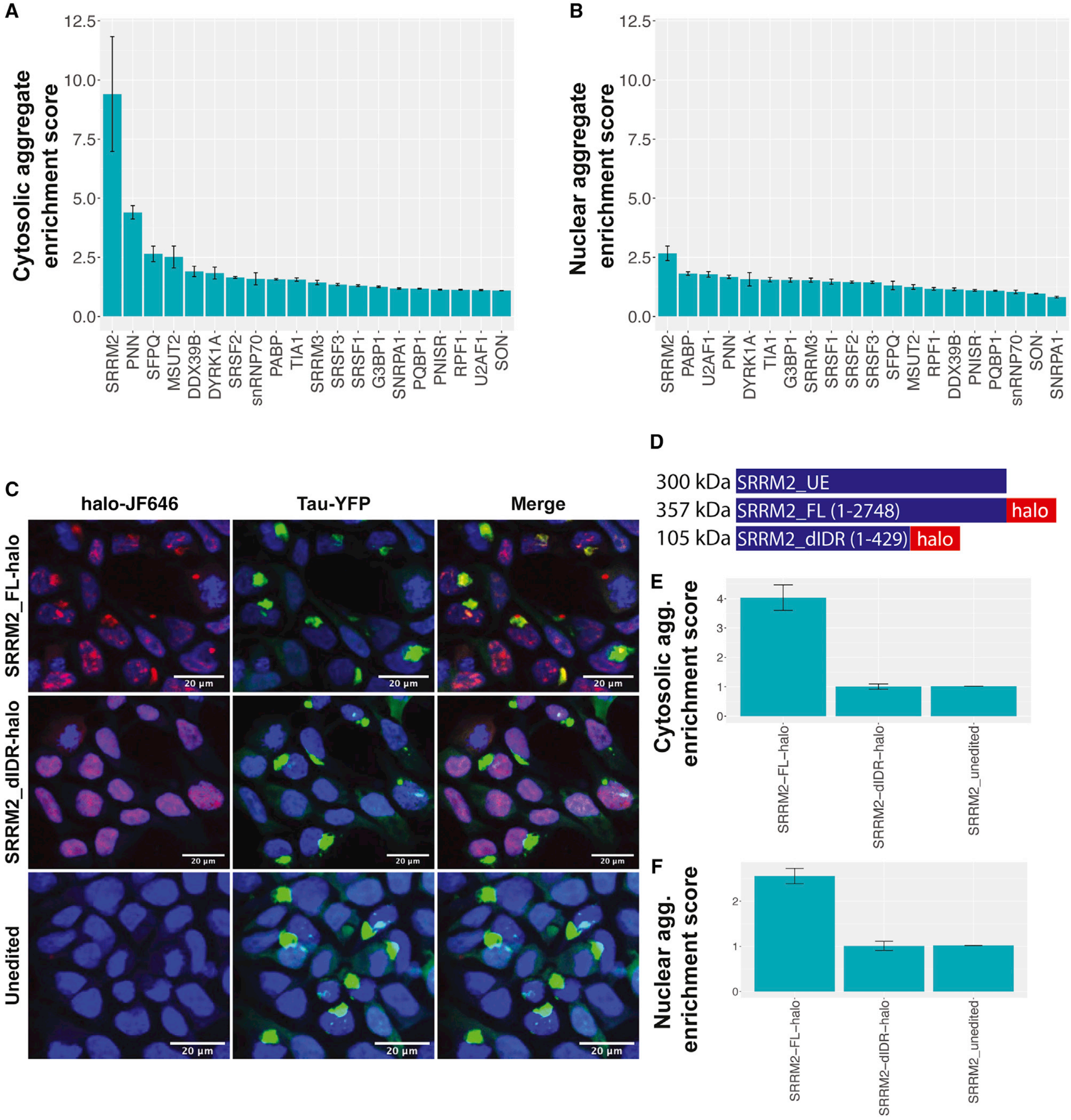

Figure 5. Other proteins that localize to tau aggregates and the C-terminal region of SRRM2 are responsible for localization to tau aggregates

(A and B) Cytosolic and nuclear tau aggregate enrichment scores (median intensity within tau aggregate/median intensity within cytosol or nucleus) for 20 proteins. Ilastik was used to segment images into the following categories: nuclear tau aggregates, cytosolic tau aggregates, nucleus, cytosol, and background. Segmentation masks and raw images were used as input into CellProfiler to quantify the median intensity of the interrogated protein Data are represented as mean ± 95% confidence interval (n = 25 images per condition).

(C) Images of cell CRISPR-edited to express endogenous FL or dIDR SRRM2 tagged with halo.

(D) Schematic of SRRM2 constructs.

(E and F) Cytosolic and nuclear enrichment scores for FL-halo, dIDR-halo, and unedited SRRM2. Data are represented as mean ± 95% confidence interval (n = 25 images per condition).

See also Figure S5.

Please cite this article in press as: Lester et al., Tau aggregates are RNA-protein assemblies that mislocalize multiple nuclear speckle components, Neuron (2021), https://doi.org/10.1016/j.neuron.2021.03.026

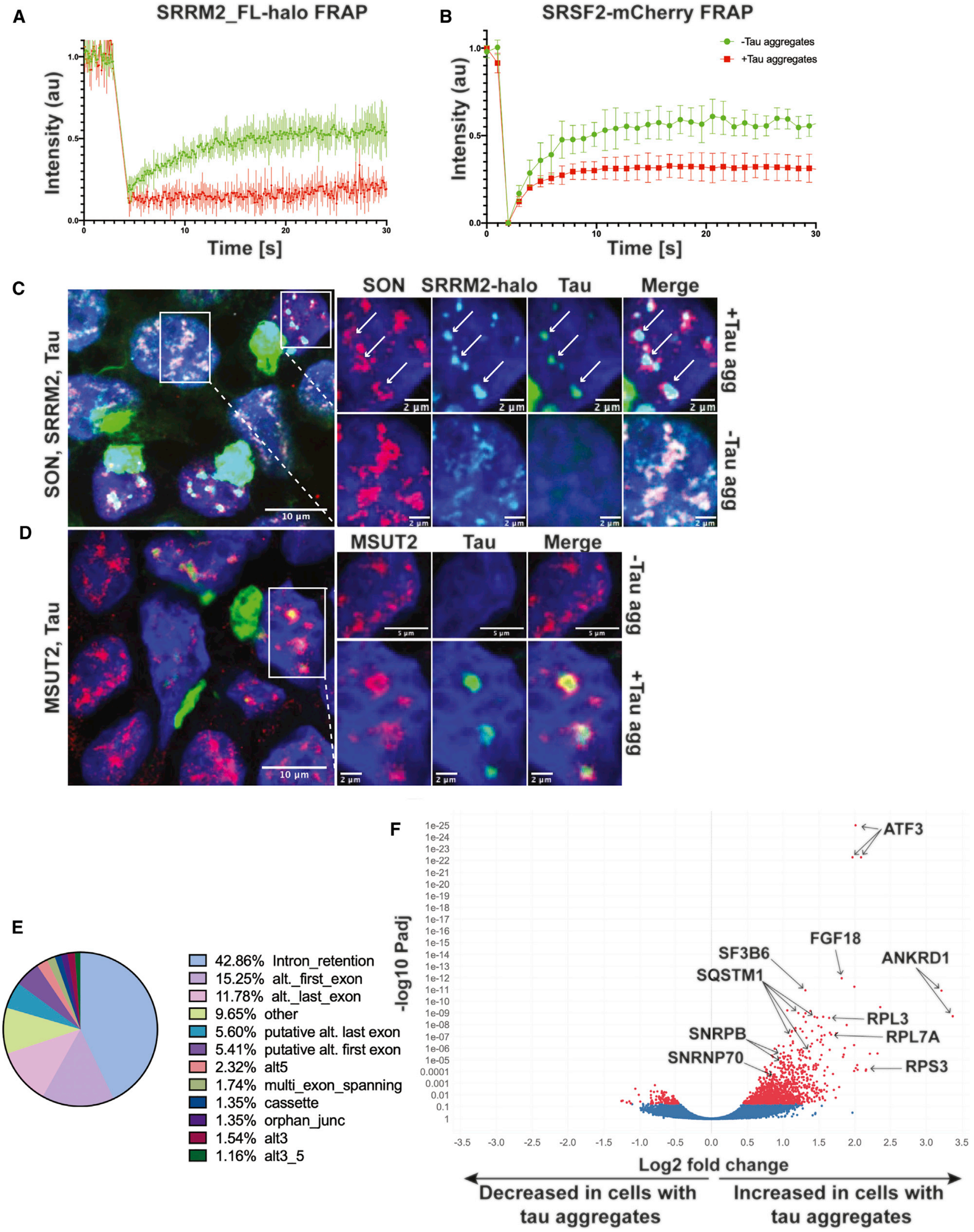

(legend on next page)

Examination of the types of local splicing variations revealed that the largest categories were intron retention (42.86%), alternative first exons (15.25%), and alternative last exons (11.78%) (Figure 6E; MAJIQ splicing diagrams and IGV raw read counts for one example, ATF3, are provided in Figures S6A and S6B). Because of the abundance of intron retention events, we used iREAD to better quantify differential intron retention between cells with and without tau aggregates. Reads that fully or partially overlap annotated introns were then used for differential expression analysis using DEseq2 (Li et al., 2020; Love et al., 2014). We found that, at Padj < 0.05, there were 1,225 introns in 641 genes that were retained in cells with tau aggregates and 120 introns in 86 genes that were retained in cells without tau aggregates (Figure 6F). Pre-mRNAs with retained introns in cells with tau aggregates cluster in genes affecting the apoptosis and splicing associated protein (ASAP) complex, ribosome, and RNA splicing and processing (Figure S6C). Thus, formation of tau aggregates in cells is sufficient to induce changes in pre-mRNA splicing and is expected to have significant biological effects. Because individuals with tauopathies and model systems with tau mutations show changes in pre-mRNA splicing patterns in the brain (Apicco et al., 2019; Hsieh et al., 2019; Raj et al., 2018), an alteration in splicing because of tau aggregate formation may contribute to these splicing changes (see Discussion).

SRRM2 is depleted from the nucleus and relocalized to cytosolic tau neurofibrillary tangles in mouse and human tauopathies

Because SRRM2 was the most highly enriched protein identified in tau aggregates (Figure 5A), we examined, via IF, whether cytosolic tau aggregates also contain SRRM2 in mice, using the ab11826 antibody on brains from WT B6/J mice or Tg2541 mice. In B6 control mice, SRRM2 predominantly localized to poly(A)$^+$ nuclear speckles (Figure S7A). In contrast, we observed that SRRM2 relocalized from the nucleus into cytosolic phospho-tau aggregates in P301S-expressing Tg2541 mice (Figure S7A). Consistent with these observations, phosphorylated SRRM2 has been observed previously to be relocalized to the cytosol in 5X FAD mouse brains using a different antibody; however, the association of SRRM2 with tau aggregates has not been reported (Tanaka et al., 2018). Thus, SRRM2, and potentially other nuclear speckle components, relocalize and sequester into cytosolic tau aggregates in both cell culture models and in tauopathy mice.

To examine whether SRRM2 is mislocalized in human tauopathies, we performed IF on brains of individuals with tauopathy. We observed that, in individuals with the primary tauopathy CBD, SRRM2 was present in tau-containing cytosolic aggregates in the form of neuropil threads, whereas SRRM2 localized to nuclear speckles in aged-matched heathy control individuals (Figure 7A; demographics in Table S3). Quantification of CBD and age-matched control images revealed that the average nuclear SRRM2 signal was significantly lower in CBD brains compared with controls (Figure 7B). We also observed that SRRM2 was re-localized from the nucleus into the cytosol in the frontal cortex of multiple brains of individuals with AD and FTLD (n = 4 AD and n = 4 FTLD) but not age-matched control brains (n = 4; Figures 7C and S7B; demographics in Table S3). These results show that cytosolic SRRM2 is a histopathological feature seen across three distinct human tauopathies.

DISCUSSION

We present several lines of evidence that cytosolic and nuclear tau aggregates contain RNA. First, in mice and HEK293 cells, nuclear and cytosolic tau aggregates stained positive for poly(A) RNAs, indicating the presence of mRNAs or non-coding RNAs with poly(A) tails (Figures 1, S1D, S1E, and S7A). Second, purification and sequencing of tau aggregates from mouse brains or HEK293 cells demonstrated the presence and enrichment of specific RNAs, most notably snRNAs and snoRNAs (Figure 2). Third, FISH for specific RNAs in HEK293 cells validated that our sequencing identified RNAs enriched in tau aggregates (Figure 3). Although we have not yet examined the specific RNAs present in tau aggregates in human pathologies, tau aggregates in brains of affected individuals stain positive with acridine orange, a dye with specificity for RNA (Ginsberg et al., 1997, 1998). Based on these observations, we suggest that tau aggregates generally contain RNA and that the presence of specific RNA species may alter their structure, formation, and stability. The presence of RNA in tau aggregates may explain why tau aggregates and other RNA binding proteins can co-immunoprecipitate and/or co-localize (Apicco et al., 2018; Gunawardana et al., 2015; Hales et al., 2014a, 2014b; Maziuk et al., 2018; Meier et al., 2016; Vanderweyde et al., 2016).

We observed that tau aggregates are enriched for a number of different RNA species. Most notably, we observed enrichment of specific snRNA and snoRNAs in HEK293 reporter cells and mouse brains, although the specific snRNA/snoRNA species can vary between model systems (Figure 2). We also observed enrichment of repetitive RNAs (such as tRNAs, Alu elements, and satellite RNAs) and some mRNAs coding for proteins in the centrosome and spliceosome (Figures S2A and S2G).

Figure 6. Tau aggregation alters the dynamics and organization of nuclear speckles as well as RNA splicing

(A and B) FRAP of SRRM2_FL-halo (A) and SRSF2-mCherry (B) nuclear speckles with and without tau aggregates (n = 5 replicates). A 405-nm laser was used to photobleach, and fluorescence intensity was measured using the 647-nm channel for halo-JF647 and the 561-nm channel for mCherry. Data are represented as mean ± standard deviation.

(C and D) Images of P301S tau-transfected cells showing nuclear speckle reorganization in the presence of aggregates. SON and MSUT2 move to the periphery of nuclear speckles, whereas SRRM2 remains in the center of nuclear speckles with the tau aggregate.

(E) MAJIQ analysis of splicing changes in cells with and without tau aggregates (n = 3 biological replicates per condition), showing that intron retention constitutes the largest percentage of local splicing variations.

(F) Volcano plot showing differential intron retention in cells with tau aggregates, quantified by iREAD and DEseq2 (red, Padj < 0.05). Padj values were determined from DESeq2 using the Benjamini-Hochberg method. Multiple points per gene are due to the multiple retained introns in those genes.

See also Figure S6.

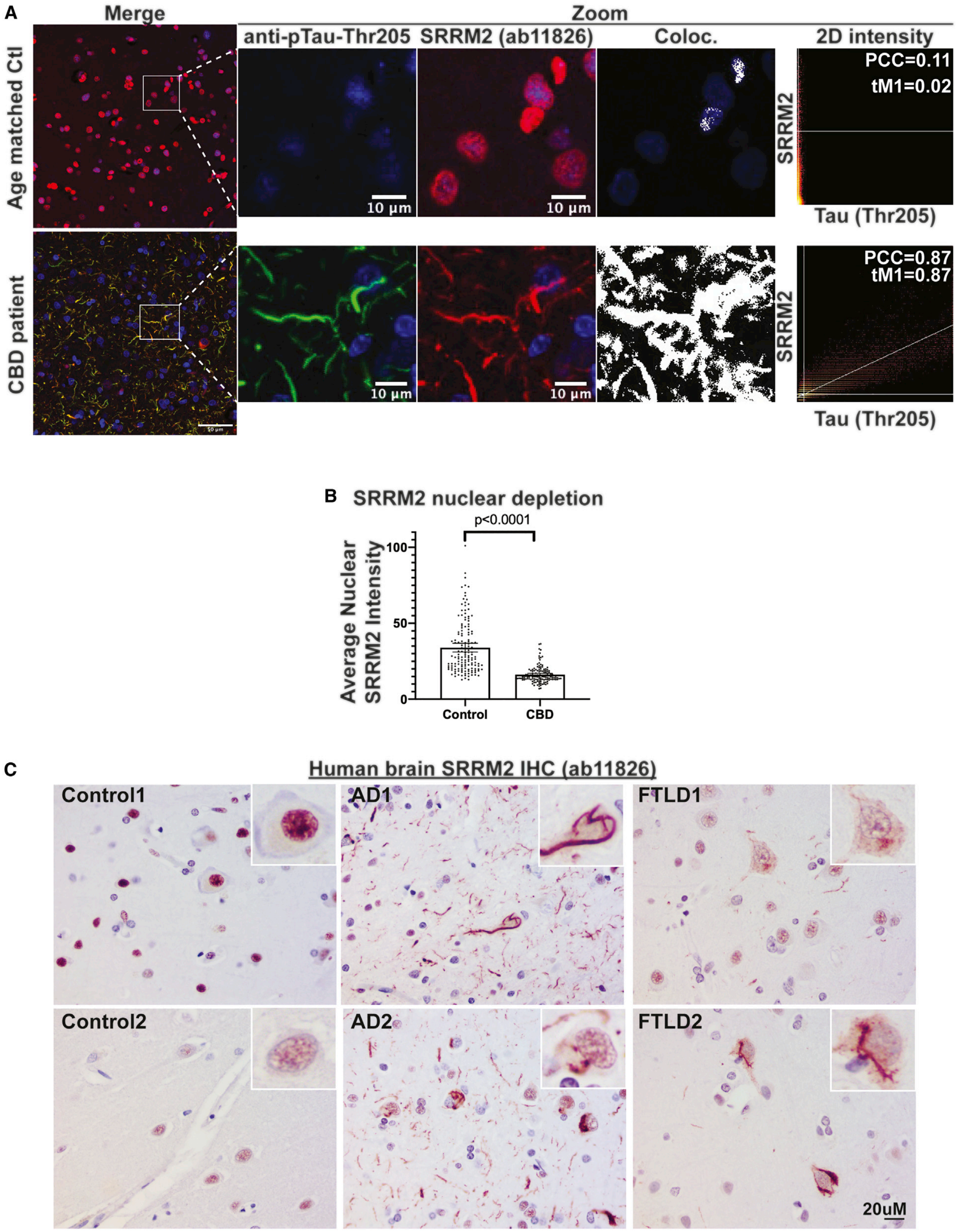

(legend on next page)

Because our library preparation protocol was not specifically designed to capture tRNAs, microRNAs (miRNAs), or rRNAs, our analyses may underestimate the abundance of these species (Motameny et al., 2010; Xu et al., 2019). The mechanisms by which specific RNAs are enriched in tau aggregates remains to be determined but could be due to tau's intrinsic RNA binding specificity, the structure of the tau conformers, and/or the presence of specific RNAs at sites of tau aggregation, such as snRNAs in nuclear speckles or mRNAs at the centrosome (Sepulveda et al., 2018). We suggest that tau aggregates in cells could be considered representative of the growing class of RNA and protein assemblies.

We provide evidence that nuclear tau aggregates form in nuclear speckles and alter their properties, composition, and function. One critical observation is that nuclear tau assemblies are observed in HEK293 cells and P301L mice that overlap with protein and RNA markers of nuclear speckles (Figures 4, S4, and S7). Moreover, nuclear speckles that contain tau aggregates show altered dynamics of SRRM2 and SRSF2 (Figure 6A), demonstrating that tau aggregation has altered their material properties. Tau accumulation in nuclear speckles also changes their spatial organization, with proteins partitioning into novel sub-domains of the assembly (Figures 6C and 6D). Finally, because cytoplasmic tau aggregates accumulate multiple components of nuclear speckles, leading to their depletion from the nucleus, the presence of tau aggregates in cells alters the composition of nuclear speckles.

A critical question is the biological significance of the nuclear tau aggregates. It is important to note that we observed tau aggregates in cell and mouse models of tauopathies, demonstrating that nuclear tau aggregates are not an artifact of cell line models (Figures 1C, S1E, and S7A). Moreover, we observed tau aggregates in nuclear speckles in HEK293 cells expressing just the 4 repeat regions of tau and in H4 neuroglioma cells expressing a full-length 0N4R tau isoform (Figure S1A), demonstrating that tau accumulating in nuclear speckles is not an artifact of expressing truncated tau. Although tau is predominantly thought to be a cytosolic microtubule-associated protein, numerous labs have observed aggregated and unaggregated tau in the nucleus of neuronal and non-neuronal cells (Bengoa-Vergniory et al., 2021; Bukar Maina et al., 2016; Gärtner et al., 1998; Gil et al., 2017; Jiang et al., 2019; Liu and Götz, 2013; Maj et al., 2010; Metuzals et al., 1988; Montalbano et al., 2020; Brady et al., 1995; Siano et al., 2019; Ulrich et al., 2018; Violet et al., 2014, 2015). One particularly interesting case report shows abundant nuclear tau (PHF-1-, Tau-1-, Tau-2-, Tau-3-, Tau-5-, and SMI-31-positive) in the brain of a 64-year-old man with pre-senile dementia and motor neuron disease whose neurologic status deteriorated rapidly prior to his death (Papasozomenos, 1995). Previous studies in HEK293 cells found that transfection of tau conformers that produced nuclear tau aggregates with a "speckled" phenotype were associated with greater cellular toxicity relative to those that only produced cytosolic tau aggregates (Sanders et al., 2014). In agreement, the suppressor of tau toxicity, MSUT2 (Guthrie et al., 2011; Wheeler et al., 2019), also localizes to nuclear speckles (Figures 6D and S5A). Thus, tau's interaction with nuclear speckle components could be integral to the toxicity of tau aggregation.

A striking feature of our results is that cytoplasmic tau aggregates accumulate and mislocalize several proteins that normally accumulate in nuclear speckles (Figures 4, 5, 6, and S4–S7). The most striking of these is the SRRM2 protein, which can show an order of magnitude enrichment in cytosolic tau aggregates compared with bulk cytosol (Figure 5A). Moreover, we also observed accumulation of SRRM2 in tau aggregates in mice and in the human tauopathy CBD (Figure 7A). Strikingly, we observed cytosolic mislocalization and/or nuclear depletion of SRRM2 in multiple tauopathies, including AD and FTLD (Figures 7C and S7B). The consistent mislocalization of SRRM2 in cell line and animal models of tauopathy as well as in postmortem brain samples from affected individuals argues that mislocalization of nuclear speckle proteins into cytosolic tau aggregates is a fundamental and consistent consequence of tau aggregation. An important issue for future work is to determine the mechanism of nuclear speckle component mislocalization.

One likely consequence of altering the composition and dynamics of nuclear speckles would be to alter pre-mRNA splicing. It is well documented that pre-mRNA splicing is altered in brains of individuals with tauopathy, including individuals with AD (Hsieh et al., 2019; Raj et al., 2018). Consistent with this finding, we demonstrate that formation of tau aggregates in HEK293 cells is sufficient to induce alterations in alternative splicing and increase the number of significantly retained introns (Figures 6E, 6F, and S6). Thus, tau aggregates are sufficient to alter pre-mRNA splicing, although it should be noted that splicing alterations seen in diseased tissue may be complicated by additional factors, including multiple cell types and neuroinflammatory responses. Interestingly, many of these retained introns triggered by tau aggregates are in RNAs that code for proteins involved in RNA processing and ribosome biogenesis (Figure S6C). Disruption of these processes could lead to a pathologic cascade, potentially explaining the complex alterations in ribosome function and RNA processing that have been observed in individuals with AD (Hsieh et al., 2019; Ding et al., 2005; Raj et al., 2018). These results raise the possibility that tau aggregation per se is responsible for some of the splicing changes seen in disease tissue.

The coaggregation of RNA and proteins in tauopathies is reminiscent of pathologic RNA-protein aggregates seen in other

Figure 7. SRRM2 is relocalized to cytosolic tau aggregates in human tauopathies

(A) IF and colocalization analysis showing that hyperphosphorylated tau (pTau-Thr205, MN1020) colocalizes with SRRM2 (ab11826) in the cytosol of a brain of an individual with CBD, whereas SRRM2 is localized to the nucleus in an age-matched control brain.

(B) Quantification of the average nuclear SRRM2 intensity, showing a significant decrease in the setting of CBD relative to an age-matched control. Data are represented as mean ± 95% confidence interval, and p values were determined using a Mann-Whitney test (n = 135 nuclei). Immunohistochemistry of SRRM2 in human brains shows SRRM2 redistribution to the cytosol in AD and FTD brains but retains nuclear localization in control brains. Sample information and additional examples can be found in Figure S7B and Table S3.

See also Figure S7.

neurodegenerative and neuromuscular diseases, such as ALS and inclusion body myopathy (Ramaswami et al., 2013; Taylor et al., 2016). Thus, the sequestration of RNAs and RNA binding proteins into pathologic aggregates may represent a shared pathophysiological feature across multiple degenerative diseases affecting diverse tissue types, with a common feature being depletion of critical RNA processing factors from the nucleus leading to changes in RNA processing and gene expression.

STAR★METHODS

Detailed methods are provided in the online version of this paper and include the following:

- KEY RESOURCES TABLE
- RESOURCE AVAILABILITY
  - ○ Lead contact
  - ○ Materials availability
  - ○ Data and code availability
- EXPERIMENTAL MODEL AND SUBJECT DETAILS
  - ○ Tauopathy mouse models
  - ○ Cell culture and tau seeding of H4 biosensor cells
  - ○ Cell culture and tau seeding in HEK293 biosensor cells
- METHOD DETAILS
  - ○ Clarification of brain homogenate for tau aggregate seeding in HEK293 cells
  - ○ PTA precipitation from brain homogenate for tau aggregate seeding in H4 biosensor cells
  - ○ Fluorescent labeling of oligonucleotides for FISH
  - ○ Tau aggregate isolation from HEK293 cells via centrifugation and flow cytometry
  - ○ Isolation of tau aggregates from mouse brain
  - ○ Generation of Lentiviral particles
  - ○ Generating SRSF2-mCherry cells via lenti-virus
  - ○ Generating halo tagged SRRM2 cells using CRISPaint
  - ○ Immunofluorescence (IF) in HEK293 and H4 cells
  - ○ Fluorescence *in situ* hybridization (FISH)
  - ○ Fluorescence recovery after photobleaching
  - ○ Mouse brain RNA fluorescent *in situ* hybridization followed by immunofluorescent staining (RNA FISH-IF)
  - ○ Human brain immunofluorescent staining
  - ○ Human tissue samples for immunohistochemistry
  - ○ Immunohistochemistry
- QUANTIFICATION AND STATISTICAL ANALYSIS
  - ○ Image analysis
  - ○ Analysis of RNA sequencing data

SUPPLEMENTAL INFORMATION

Supplemental information can be found online at https://doi.org/10.1016/j.neuron.2021.03.026.

ACKNOWLEDGMENTS

We would like to thank Joe Dragavon, PhD, for assistance with microscopy at the BioFrontiers Advanced Light Microscopy Core (supported by NIST-CU 70NANB15H226); Theresa Nahreini for assistance at the Biochemistry Cell Culture Facility at CU Boulder; and the BioFrontiers Institute Next-Gen Sequencing Core Facility, which performed Illumina sequencing and library construction. We would also like to thank Dr. James Burke for assistance and discussions regarding experimental design. This work was supported by grants from the National Institutes of Health (NIH; 1F30AG063468-01 to E.L., 5R01GM045443-31 to R.P., and 2P01AG002132-39 to S.B.P.), the Brockman Foundation (to S.B.P.), the Sherman Fairchild Foundation (to S.B.P.), and the Howard Hughes Medical Institute (to R.P.).

AUTHOR CONTRIBUTIONS

E.L., A.L.W., F.K.O., G.A.C., S.B.P., and R.P. conceived and designed the research. E.L. and R.P. wrote the manuscript. All authors edited drafts. E.L. performed sequencing data analysis, image data analysis, and all HEK293 tau biosensor cell experiments. A.L.W. and G.A.C. set up mouse experiments and isolated mouse tissue for tau aggregate isolation. F.K.O. performed staining in CBD brains and mouse brain tissue and performed H4 cell experiments. J.A. created the H4 neuroglioma cell line. N.B. and R.B. performed IHC on human tissue sections for SRRM2.

DECLARATION OF INTERESTS

R.P. is a founder and consultant for Faze Medicines. S.B.P. is a member of the Scientific Advisory Boards of ViewPoint Therapeutics and New Ventures Inc. and a member of the Supervisory Board of Priavoid, none of which have contributed financial or any other support to these studies.

Received: August 7, 2020
Revised: February 5, 2021
Accepted: March 18, 2021
Published: April 12, 2021

REFERENCES

Allen, B., Ingram, E., Takao, M., Smith, M.J., Jakes, R., Virdee, K., Yoshida, H., Holzer, M., Craxton, M., Emson, P.C., et al. (2002). Abundant tau filaments and nonapoptotic neurodegeneration in transgenic mice expressing human P301S tau protein. J. Neurosci. *22*, 9340–9351.

Ambadipudi, S., Biernat, J., Riedel, D., Mandelkow, E., and Zweckstetter, M. (2017). Liquid-liquid phase separation of the microtubule-binding repeats of the Alzheimer-related protein Tau. Nat. Commun. *8*, 275.

Aoyagi, A., Condello, C., Stöhr, J., Yue, W., Rivera, B.M., Lee, J.C., Woerman, A.L., Halliday, G., van Duinen, S., Ingelsson, M., et al. (2019). Aβ and tau prion-like activities decline with longevity in the Alzheimer's disease human brain. Sci. Transl. Med. *11*, eaat8462.

Apicco, D.J., Ash, P.E.A., Maziuk, B., LeBlang, C., Medalla, M., Al Abdullatif, A., Ferragud, A., Botelho, E., Ballance, H.I., Dhawan, U., et al. (2018). Reducing the RNA binding protein TIA1 protects against tau-mediated neurodegeneration in vivo. Nat. Neurosci. *21*, 72–80.

Apicco, D.J., Zhang, C., Maziuk, B., Jiang, L., Ballance, H.I., Boudeau, S., Ung, C., Li, H., and Wolozin, B. (2019). Dysregulation of RNA Splicing in Tauopathies. Cell Rep. *29*, 4377–4388.e4.

Bai, B., Hales, C.M., Chen, P.-C., Gozal, Y., Dammer, E.B., Fritz, J.J., Wang, X., Xia, Q., Duong, D.M., Street, C., et al. (2013). U1 small nuclear ribonucleoprotein complex and RNA splicing alterations in Alzheimer's disease. Proc. Natl. Acad. Sci. USA *110*, 16562–16567.

Bengoa-Vergniory, N., Velentza-Almpani, E., Silva, A.M., Scott, C., Vargas-Caballero, M., Sastre, M., Wade-Martins, R., and Alegre-Abarrategui, J. (2021). Tau-proximity ligation assay reveals extensive previously undetected pathology prior to neurofibrillary tangles in preclinical Alzheimer's disease. Acta Neuropathol. Commun. *9*, 18.

Berg, S., Kutra, D., Kroeger, T., Straehle, C.N., Kausler, B.X., Haubold, C., Schiegg, M., Ales, J., Beier, T., Rudy, M., et al. (2019). ilastik: interactive machine learning for (bio)image analysis. Nat. Methods *16*, 1226–1232.

Bolger, A.M., Lohse, M., and Usadel, B. (2014). Trimmomatic: a flexible trimmer for Illumina sequence data. Bioinformatics *30*, 2114–2120.

Brady, R.M., Zinkowski, R.P., and Binder, L.I. (1995). Presence of tau in isolated nuclei from human brain. Neurobiol. Aging *16*, 479–486.

Please cite this article in press as: Lester et al., Tau aggregates are RNA-protein assemblies that mislocalize multiple nuclear speckle components, Neuron (2021), https://doi.org/10.1016/j.neuron.2021.03.026

Brandt, R., Léger, J., and Lee, G. (1995). Interaction of tau with the neural plasma membrane mediated by tau's amino-terminal projection domain. J. Cell Biol. *131*, 1327–1340.

Broccolini, A., Engel, W.K., Alvarez, R.B., and Askanas, V. (2000). Paired helical filaments of inclusion-body myositis muscle contain RNA and survival motor neuron protein. Am. J. Pathol. *156*, 1151–1155.

Buée, L., Bussière, T., Buée-Scherrer, V., Delacourte, A., and Hof, P.R. (2000). Tau protein isoforms, phosphorylation and role in neurodegenerative disorders. Brain Res. Brain Res. Rev. *33*, 95–130.

Bukar Maina, M., Al-Hilaly, Y.K., and Serpell, L.C. (2016). Nuclear Tau and Its Potential Role in Alzheimer's Disease. Biomolecules *6*, 9.

Burke, J.M., Moon, S.L., Matheny, T., and Parker, R. (2019). RNase L Reprograms Translation by Widespread mRNA Turnover Escaped by Antiviral mRNAs. Mol. Cell *75*, 1203–1217.e5.

Campeau, E., Ruhl, V.E., Rodier, F., Smith, C.L., Rahmberg, B.L., Fuss, J.O., Campisi, J., Yaswen, P., Cooper, P.K., and Kaufman, P.D. (2009). A versatile viral system for expression and depletion of proteins in mammalian cells. PLoS ONE *4*, e6529.

Chen, J., Kanai, Y., Cowan, N.J., and Hirokawa, N. (1992). Projection domains of MAP2 and tau determine spacings between microtubules in dendrites and axons. Nature *360*, 674–677.

Criscione, S.W., Zhang, Y., Thompson, W., Sedivy, J.M., and Neretti, N. (2014). Transcriptional landscape of repetitive elements in normal and cancer human cells. BMC Genomics *15*, 583.

Delaval, B., and Doxsey, S.J. (2010). Pericentrin in cellular function and disease. J. Cell Biol. *188*, 181–190.

DeVos, S.L., Corjuc, B.T., Commins, C., Dujardin, S., Bannon, R.N., Corjuc, D., Moore, B.D., Bennett, R.E., Jorfi, M., Gonzales, J.A., et al. (2018). Tau reduction in the presence of amyloid-β prevents tau pathology and neuronal death in vivo. Brain *141*, 2194–2212.

Diner, I., Nguyen, T., and Seyfried, N.T. (2017). Enrichment of Detergent-insoluble Protein Aggregates from Human Postmortem Brain. J. Vis. Exp. (128).

Ding, Q., Markesbery, W.R., Chen, Q., Li, F., and Keller, J.N. (2005). Ribosome dysfunction is an early event in Alzheimer's disease. J. Neurosci. *25*, 9171–9175.

Dinkel, P.D., Holden, M.R., Matin, N., and Margittai, M. (2015). RNA Binds to Tau Fibrils and Sustains Template-Assisted Growth. Biochemistry *54*, 4731–4740.

Dobin, A., Davis, C.A., Schlesinger, F., Drenkow, J., Zaleski, C., Jha, S., Batut, P., Chaisson, M., and Gingeras, T.R. (2013). STAR: ultrafast universal RNA-seq aligner. Bioinformatics *29*, 15–21.

Falcon, B., Zhang, W., Murzin, A.G., Murshudov, G., Garringer, H.J., Vidal, R., Crowther, R.A., Ghetti, B., Scheres, S.H.W., and Goedert, M. (2018). Structures of filaments from Pick's disease reveal a novel tau protein fold. Nature *561*, 137–140.

Falcon, B., Zivanov, J., Zhang, W., Murzin, A.G., Garringer, H.J., Vidal, R., Crowther, R.A., Newell, K.L., Ghetti, B., Goedert, M., and Scheres, S.H.W. (2019). Novel tau filament fold in chronic traumatic encephalopathy encloses hydrophobic molecules. Nature *568*, 420–423.

Fitzpatrick, A.W.P., Falcon, B., He, S., Murzin, A.G., Murshudov, G., Garringer, H.J., Crowther, R.A., Ghetti, B., Goedert, M., and Scheres, S.H.W. (2017). Cryo-EM structures of tau filaments from Alzheimer's disease. Nature *547*, 185–190.

Galganski, L., Urbanek, M.O., and Krzyzosiak, W.J. (2017). Nuclear speckles: molecular organization, biological function and role in disease. Nucleic Acids Res. *45*, 10350–10368.

Gärtner, U., Janke, C., Holzer, M., Vanmechelen, E., and Arendt, T. (1998). Postmortem changes in the phosphorylation state of tau-protein in the rat brain. Neurobiol. Aging *19*, 535–543.

Gaspar, I., Wippich, F., and Ephrussi, A. (2017). Enzymatic production of single-molecule FISH and RNA capture probes. RNA *23*, 1582–1591.

Gil, L., Federico, C., Pinedo, F., Bruno, F., Rebolledo, A.B., Montoya, J.J., Olazabal, I.M., Ferrer, I., and Saccone, S. (2017). Aging dependent effect of nuclear tau. Brain Res. *1677*, 129–137.

Ginsberg, S.D., Crino, P.B., Lee, V.M., Eberwine, J.H., and Trojanowski, J.Q. (1997). Sequestration of RNA in Alzheimer's disease neurofibrillary tangles and senile plaques. Ann. Neurol. *41*, 200–209.

Ginsberg, S.D., Galvin, J.E., Chiu, T.S., Lee, V.M., Masliah, E., and Trojanowski, J.Q. (1998). RNA sequestration to pathological lesions of neurodegenerative diseases. Acta Neuropathol. *96*, 487–494.

Goedert, M. (2005). Tau gene mutations and their effects. Mov. Disord. *20* (*Suppl 12*), S45–S52.

Goedert, M., and Spillantini, M.G. (2000). Tau mutations in frontotemporal dementia FTDP-17 and their relevance for Alzheimer's disease. Biochim. Biophys. Acta *1502*, 110–121.

Goedert, M., Wischik, C.M., Crowther, R.A., Walker, J.E., and Klug, A. (1988). Cloning and sequencing of the cDNA encoding a core protein of the paired helical filament of Alzheimer disease: identification as the microtubule-associated protein tau. Proc. Natl. Acad. Sci. USA *85*, 4051–4055.

Grainger, R.J., Barrass, J.D., Jacquier, A., Rain, J.-C., and Beggs, J.D. (2009). Physical and genetic interactions of yeast Cwc21p, an ortholog of human SRm300/SRRM2, suggest a role at the catalytic center of the spliceosome. RNA *15*, 2161–2173.

Graser, S., Stierhof, Y.-D., Lavoie, S.B., Gassner, O.S., Lamla, S., Le Clech, M., and Nigg, E.A. (2007). Cep164, a novel centriole appendage protein required for primary cilium formation. J. Cell Biol. *179*, 321–330.

Gunawardana, C.G., Mehrabian, M., Wang, X., Mueller, I., Lubambo, I.B., Jonkman, J.E.N., Wang, H., and Schmitt-Ulms, G. (2015). The Human Tau Interactome: Binding to the Ribonucleoproteome, and Impaired Binding of the Proline-to-Leucine Mutant at Position 301 (P301L) to Chaperones and the Proteasome. Mol. Cell. Proteomics *14*, 3000–3014.

Guthrie, C.R., Greenup, L., Leverenz, J.B., and Kraemer, B.C. (2011). MSUT2 is a determinant of susceptibility to tau neurotoxicity. Hum. Mol. Genet. *20*, 1989–1999.

Hales, C.M., Dammer, E.B., Diner, I., Yi, H., Seyfried, N.T., Gearing, M., Glass, J.D., Montine, T.J., Levey, A.I., and Lah, J.J. (2014a). Aggregates of small nuclear ribonucleic acids (snRNAs) in Alzheimer's disease. Brain Pathol. *24*, 344–351.

Hales, C.M., Seyfried, N.T., Dammer, E.B., Duong, D., Yi, H., Gearing, M., Troncoso, J.C., Mufson, E.J., Thambisetty, M., Levey, A.I., and Lah, J.J. (2014b). U1 small nuclear ribonucleoproteins (snRNPs) aggregate in Alzheimer's disease due to autosomal dominant genetic mutations and trisomy 21. Mol. Neurodegener. *9*, 15.

Hanseeuw, B.J., Betensky, R.A., Jacobs, H.I.L., Schultz, A.P., Sepulcre, J., Becker, J.A., Cosio, D.M.O., Farrell, M., Quiroz, Y.T., Mormino, E.C., et al. (2019). Association of Amyloid and Tau With Cognition in Preclinical Alzheimer Disease: A Longitudinal Study. JAMA Neurol. *76*, 915–924.

Holmes, B.B., Furman, J.L., Mahan, T.E., Yamasaki, T.R., Mirbaha, H., Eades, W.C., Belaygorod, L., Cairns, N.J., Holtzman, D.M., and Diamond, M.I. (2014). Proteopathic tau seeding predicts tauopathy in vivo. Proc. Natl. Acad. Sci. USA *111*, E4376–E4385.

Hoover, B.R., Reed, M.N., Su, J., Penrod, R.D., Kotilinek, L.A., Grant, M.K., Pitstick, R., Carlson, G.A., Lanier, L.M., Yuan, L.-L., et al. (2010). Tau mislocalization to dendritic spines mediates synaptic dysfunction independently of neurodegeneration. Neuron *68*, 1067–1081.

Hsieh, Y.-C., Guo, C., Yalamanchili, H.K., Abreha, M., Al-Ouran, R., Li, Y., Dammer, E.B., Lah, J.J., Levey, A.I., Bennett, D.A., et al. (2019). Tau-Mediated Disruption of the Spliceosome Triggers Cryptic RNA Splicing and Neurodegeneration in Alzheimer's Disease. Cell Rep. *29*, 301–316.e10.

Huang, S., Deerinck, T.J., Ellisman, M.H., and Spector, D.L. (1994). In vivo analysis of the stability and transport of nuclear poly(A)+ RNA. J. Cell Biol. *126*, 877–899.

Ilik, İ.A., Malszycki, M., Lübke, A.K., Schade, C., Meierhofer, D., and Aktaş, T. (2020). SON and SRRM2 are essential for nuclear speckle formation. eLife *9*, e60579.

Jiang, L., Ash, P.E.A., Maziuk, B.F., Ballance, H.I., Boudeau, S., Abdullatif, A.A., Orlando, M., Petrucelli, L., Ikezu, T., and Wolozin, B. (2019). TIA1 regulates the generation and response to toxic tau oligomers. Acta Neuropathol. *137*, 259–277.

Johnson, N.R., Condello, C., Guan, S., Oehler, A., Becker, J., Gavidia, M., Carlson, G.A., Giles, K., and Prusiner, S.B. (2017). Evidence for sortilin modulating regional accumulation of human tau prions in transgenic mice. Proc. Natl. Acad. Sci. USA *114*, E11029–E11036.

Kampers, T., Friedhoff, P., Biernat, J., Mandelkow, E.M., and Mandelkow, E. (1996). RNA stimulates aggregation of microtubule-associated protein tau into Alzheimer-like paired helical filaments. FEBS Lett. *399*, 344–349.

Kaufman, S.K., Sanders, D.W., Thomas, T.L., Ruchinskas, A.J., Vaquer-Alicea, J., Sharma, A.M., Miller, T.M., and Diamond, M.I. (2016). Tau Prion Strains Dictate Patterns of Cell Pathology, Progression Rate, and Regional Vulnerability In Vivo. Neuron *92*, 796–812.

Khong, A., Matheny, T., Jain, S., Mitchell, S.F., Wheeler, J.R., and Parker, R. (2017). The Stress Granule Transcriptome Reveals Principles of mRNA Accumulation in Stress Granules. Mol. Cell *68*, 808–820.e5.

Kinsella, R.J., Kähäri, A., Haider, S., Zamora, J., Proctor, G., Spudich, G., Almeida-King, J., Staines, D., Derwent, P., Kerhornou, A., et al. (2011). Ensembl BioMarts: a hub for data retrieval across taxonomic space. Database (Oxford) *2011*, bar030.

Kiss, T. (2002). Small nucleolar RNAs: an abundant group of noncoding RNAs with diverse cellular functions. Cell *109*, 145–148.

Kota, K.P., Wagner, S.R., Huerta, E., Underwood, J.M., and Nickerson, J.A. (2008). Binding of ATP to UAP56 is necessary for mRNA export. J. Cell Sci. *121*, 1526–1537.

Lagier-Tourenne, C., Polymenidou, M., Hutt, K.R., Vu, A.Q., Baughn, M., Huelga, S.C., Clutario, K.M., Ling, S.-C., Liang, T.Y., Mazur, C., et al. (2012). Divergent roles of ALS-linked proteins FUS/TLS and TDP-43 intersect in processing long pre-mRNAs. Nat. Neurosci. *15*, 1488–1497.

Lee, G., Newman, S.T., Gard, D.L., Band, H., and Panchamoorthy, G. (1998). Tau interacts with src-family non-receptor tyrosine kinases. J. Cell Sci. *111*, 3167–3177.

Li, H.-D., Funk, C.C., and Price, N.D. (2020). iREAD: a tool for intron retention detection from RNA-seq data. BMC Genomics *21*, 128.

Liu, C., and Götz, J. (2013). Profiling murine tau with 0N, 1N and 2N isoform-specific antibodies in brain and peripheral organs reveals distinct subcellular localization, with the 1N isoform being enriched in the nucleus. PLoS ONE *8*, e84849.

Love, M.I., Huber, W., and Anders, S. (2014). Moderated estimation of fold change and dispersion for RNA-seq data with DESeq2. Genome Biol. *15*, 550.

Maj, M., Gartner, W., Ilhan, A., Neziri, D., Attems, J., and Wagner, L. (2010). Expression of TAU in insulin-secreting cells and its interaction with the calcium-binding protein secretagogin. J. Endocrinol. *205*, 25–36.

Maziuk, B.F., Apicco, D.J., Cruz, A.L., Jiang, L., Ash, P.E.A., da Rocha, E.L., Zhang, C., Yu, W.H., Leszyk, J., Abisambra, J.F., et al. (2018). RNA binding proteins co-localize with small tau inclusions in tauopathy. Acta Neuropathol. Commun. *6*, 71.

McQuin, C., Goodman, A., Chernyshev, V., Kamentsky, L., Cimini, B.A., Karhohs, K.W., Doan, M., Ding, L., Rafelski, S.M., Thirstrup, D., et al. (2018). CellProfiler 3.0: Next-generation image processing for biology. PLoS Biol. *16*, e2005970.

Meier, S., Bell, M., Lyons, D.N., Rodriguez-Rivera, J., Ingram, A., Fontaine, S.N., Mechas, E., Chen, J., Wolozin, B., LeVine, H., 3rd, et al. (2016). Pathological Tau Promotes Neuronal Damage by Impairing Ribosomal Function and Decreasing Protein Synthesis. J. Neurosci. *36*, 1001–1007.

Metuzals, J., Robitaille, Y., Houghton, S., Gauthier, S., and Leblanc, R. (1988). Paired helical filaments and the cytoplasmic-nuclear interface in Alzheimer's disease. J. Neurocytol. *17*, 827–833.

Montalbano, M., McAllen, S., Puangmalai, N., Sengupta, U., Bhatt, N., Johnson, O.D., Kharas, M.G., and Kayed, R. (2020). RNA-binding proteins Musashi and tau soluble aggregates initiate nuclear dysfunction. Nat. Commun. *11*, 4305.

Motameny, S., Wolters, S., Nürnberg, P., and Schumacher, B. (2010). Next Generation Sequencing of miRNAs - Strategies, Resources and Methods. Genes (Basel) *1*, 70–84.

Orr, M.E., Sullivan, A.C., and Frost, B. (2017). A Brief Overview of Tauopathy: Causes, Consequences, and Therapeutic Strategies. Trends Pharmacol. Sci. *38*, 637–648.

Papasozomenos, S.C. (1995). Nuclear tau immunoreactivity in presenile dementia with motor neuron disease: a case report. Clin. Neuropathol. *14*, 100–104.

Park, S.A., Ahn, S.I., and Gallo, J.-M. (2016). Tau mis-splicing in the pathogenesis of neurodegenerative disorders. BMB Rep. *49*, 405–413.

Polymenidou, M., Lagier-Tourenne, C., Hutt, K.R., Huelga, S.C., Moran, J., Liang, T.Y., Ling, S.-C., Sun, E., Wancewicz, E., Mazur, C., et al. (2011). Long pre-mRNA depletion and RNA missplicing contribute to neuronal vulnerability from loss of TDP-43. Nat. Neurosci. *14*, 459–468.

Raj, T., Li, Y.I., Wong, G., Humphrey, J., Wang, M., Ramdhani, S., Wang, Y.-C., Ng, B., Gupta, I., Haroutunian, V., et al. (2018). Integrative transcriptome analyses of the aging brain implicate altered splicing in Alzheimer's disease susceptibility. Nat. Genet. *50*, 1584–1592.

Ramaswami, M., Taylor, J.P., and Parker, R. (2013). Altered ribostasis: RNA-protein granules in degenerative disorders. Cell *154*, 727–736.

Ramsden, M., Kotilinek, L., Forster, C., Paulson, J., McGowan, E., SantaCruz, K., Guimaraes, A., Yue, M., Lewis, J., Carlson, G., et al. (2005). Age-dependent neurofibrillary tangle formation, neuron loss, and memory impairment in a mouse model of human tauopathy (P301L). J. Neurosci. *25*, 10637–10647.

Rino, J., Carvalho, T., Braga, J., Desterro, J.M.P., Lührmann, R., and Carmo-Fonseca, M. (2007). A stochastic view of spliceosome assembly and recycling in the nucleus. PLoS Comput. Biol. *3*, 2019–2031.

Sanders, D.W., Kaufman, S.K., DeVos, S.L., Sharma, A.M., Mirbaha, H., Li, A., Barker, S.J., Foley, A.C., Thorpe, J.R., Serpell, L.C., et al. (2014). Distinct tau prion strains propagate in cells and mice and define different tauopathies. Neuron *82*, 1271–1288.

Santa-Maria, I., Varghese, M., Ksiezak-Reding, H., Dzhun, A., Wang, J., and Pasinetti, G.M. (2012). Paired helical filaments from Alzheimer disease brain induce intracellular accumulation of Tau protein in aggresomes. J. Biol. Chem. *287*, 20522–20533.

Schmid-Burgk, J.L., Höning, K., Ebert, T.S., and Hornung, V. (2016). CRISPaint allows modular base-specific gene tagging using a ligase-4-dependent mechanism. Nat. Commun. *7*, 12338.

Schröder, H.C., Bernd, A., Zahn, R.K., and Müller, W.E. (1984). Binding of polyribonucleotides and polydeoxyribonucleotides to bovine brain microtubule protein: age-dependent modulation via phosphorylation of high-molecular-weight microtubule-associated proteins and tau proteins. Mech. Ageing Dev. *24*, 101–117.

Sepulveda, G., Antkowiak, M., Brust-Mascher, I., Mahe, K., Ou, T., Castro, N.M., Christensen, L.N., Cheung, L., Jiang, X., Yoon, D., et al. (2018). Co-translational protein targeting facilitates centrosomal recruitment of PCNT during centrosome maturation in vertebrates. eLife *7*, e34959.

Siano, G., Varisco, M., Caiazza, M.C., Quercioli, V., Mainardi, M., Ippolito, C., Cattaneo, A., and Di Primio, C. (2019). Tau Modulates VGluT1 Expression. J. Mol. Biol. *431*, 873–884.

Spector, D.L., and Lamond, A.I. (2011). Nuclear speckles. Cold Spring Harb. Perspect. Biol. *3*, a000646.

Tanaka, H., Kondo, K., Chen, X., Homma, H., Tagawa, K., Kerever, A., Aoki, S., Saito, T., Saido, T., Muramatsu, S.-I., et al. (2018). The intellectual disability gene PQBP1 rescues Alzheimer's disease pathology. Mol. Psychiatry *23*, 2090–2110.

Taylor, J.P., Brown, R.H., Jr., and Cleveland, D.W. (2016). Decoding ALS: from genes to mechanism. Nature *539*, 197–206.

Please cite this article in press as: Lester et al., Tau aggregates are RNA-protein assemblies that mislocalize multiple nuclear speckle components, Neuron (2021), https://doi.org/10.1016/j.neuron.2021.03.026

Ulrich, G., Salvadè, A., Boersema, P., Calì, T., Foglieni, C., Sola, M., Picotti, P., Papin, S., and Paganetti, P. (2018). Phosphorylation of nuclear Tau is modulated by distinct cellular pathways. Sci. Rep. *8*, 17702.

Vanderweyde, T., Apicco, D.J., Youmans-Kidder, K., Ash, P.E.A., Cook, C., Lummertz da Rocha, E., Jansen-West, K., Frame, A.A., Citro, A., Leszyk, J.D., et al. (2016). Interaction of tau with the RNA-Binding Protein TIA1 Regulates tau Pathophysiology and Toxicity. Cell Rep. *15*, 1455–1466.

Vaquero-Garcia, J., Barrera, A., Gazzara, M.R., González-Vallinas, J., Lahens, N.F., Hogenesch, J.B., Lynch, K.W., and Barash, Y. (2016). A new view of transcriptome complexity and regulation through the lens of local splicing variations. eLife *5*, e11752.

Violet, M., Delattre, L., Tardivel, M., Sultan, A., Chauderlier, A., Caillierez, R., Talahari, S., Nesslany, F., Lefebvre, B., Bonnefoy, E., et al. (2014). A major role for Tau in neuronal DNA and RNA protection in vivo under physiological and hyperthermic conditions. Front. Cell. Neurosci. *8*, 84.

Violet, M., Chauderlier, A., Delattre, L., Tardivel, M., Chouala, M.S., Sultan, A., Marciniak, E., Humez, S., Binder, L., Kayed, R., et al. (2015). Prefibrillar Tau oligomers alter the nucleic acid protective function of Tau in hippocampal neurons in vivo. Neurobiol. Dis. *82*, 540–551.

Wagner, S., Chiosea, S., Ivshina, M., and Nickerson, J.A. (2004). In vitro FRAP reveals the ATP-dependent nuclear mobilization of the exon junction complex protein SRm160. J. Cell Biol. *164*, 843–850.

Wang, X., Wang, D., Zhao, J., Qu, M., Zhou, X., He, H., and He, R. (2006). The proline-rich domain and the microtubule binding domain of protein tau acting as RNA binding domains. Protein Pept. Lett. *13*, 679–685.

Wegmann, S., Medalsy, I.D., Mandelkow, E., and Müller, D.J. (2013). The fuzzy coat of pathological human Tau fibrils is a two-layered polyelectrolyte brush. Proc. Natl. Acad. Sci. USA *110*, E313–E321.

Wheeler, J.M., McMillan, P., Strovas, T.J., Liachko, N.F., Amlie-Wolf, A., Kow, R.L., Klein, R.L., Szot, P., Robinson, L., Guthrie, C., et al. (2019). Activity of the poly(A) binding protein MSUT2 determines susceptibility to pathological tau in the mammalian brain. Sci. Transl. Med. *11*, eaao6545.

Wingett, S.W., and Andrews, S. (2018). FastQ Screen: A tool for multi-genome mapping and quality control. F1000Res. *7*, 1338.

Wischik, C.M., Novak, M., Thøgersen, H.C., Edwards, P.C., Runswick, M.J., Jakes, R., Walker, J.E., Milstein, C., Roth, M., and Klug, A. (1988). Isolation of a fragment of tau derived from the core of the paired helical filament of Alzheimer disease. Proc. Natl. Acad. Sci. USA *85*, 4506–4510.

Woerman, A.L., Aoyagi, A., Patel, S., Kazmi, S.A., Lobach, I., Grinberg, L.T., McKee, A.C., Seeley, W.W., Olson, S.H., and Prusiner, S.B. (2016). Tau prions from Alzheimer's disease and chronic traumatic encephalopathy patients propagate in cultured cells. Proc. Natl. Acad. Sci. USA *113*, E8187–E8196.

Xu, H., Yao, J., Wu, D.C., and Lambowitz, A.M. (2019). Improved TGIRT-seq methods for comprehensive transcriptome profiling with decreased adapter dimer formation and bias correction. Sci. Rep. *9*, 7953.

Yoshiyama, Y., Higuchi, M., Zhang, B., Huang, S.-M., Iwata, N., Saido, T.C., Maeda, J., Suhara, T., Trojanowski, J.Q., and Lee, V.M.-Y. (2007). Synapse loss and microglial activation precede tangles in a P301S tauopathy mouse model. Neuron *53*, 337–351.

Zhang, Q., Kota, K.P., Alam, S.G., Nickerson, J.A., Dickinson, R.B., and Lele, T.P. (2016). Coordinated dynamics of RNA splicing speckles in the nucleus. J. Cell. Physiol. *231*, 1269–1275.

Zhang, X., Lin, Y., Eschmann, N.A., Zhou, H., Rauch, J.N., Hernandez, I., Guzman, E., Kosik, K.S., and Han, S. (2017). RNA stores tau reversibly in complex coacervates. PLoS Biol. *15*, e2002183.

Zhang, X., Yan, C., Zhan, X., Li, L., Lei, J., and Shi, Y. (2018). Structure of the human activated spliceosome in three conformational states. Cell Res. *28*, 307–322.

Zhang, W., Tarutani, A., Newell, K.L., Murzin, A.G., Matsubara, T., Falcon, B., Vidal, R., Garringer, H.J., Shi, Y., Ikeuchi, T., et al. (2020). Novel tau filament fold in corticobasal degeneration. Nature *580*, 283–287.

Zimowska, G., Shi, J., Munguba, G., Jackson, M.R., Alpatov, R., Simmons, M.N., Shi, Y., and Sugrue, S.P. (2003). Pinin/DRS/memA interacts with SRp75, SRm300 and SRrp130 in corneal epithelial cells. Invest. Ophthalmol. Vis. Sci. *44*, 4715–4723.

Please cite this article in press as: Lester et al., Tau aggregates are RNA-protein assemblies that mislocalize multiple nuclear speckle components, Neuron (2021), https://doi.org/10.1016/j.neuron.2021.03.026

STAR★METHODS

KEY RESOURCES TABLE

REAGENT or RESOURCE	SOURCE	IDENTIFIER
Antibodies		
Mouse anti-pTau (S202, Thr205)	Invitrogen	Cat #: MN1020; RRID:AB_223647
Rabbit anti-pTau (Thr205)	Invitrogen	Cat #: 44-738G; RRID:AB_2533738
Mouse anti-pTau (Ser202, Thr205) AT8	Invitrogen	Cat #: MN1020; RRID:AB_223647
Rabbit anti-pTau (Ser422)	Abcam	Cat #: ab79415; RRID:AB_1603345
Mouse anti-Tau (Tau-12 clone)	Millipore	Cat #: MAB2241; RRID:AB_1977340
Mouse anti-SRRM2 (SC-35)	Abcam	Cat #: ab11826; RRID:AB_298608
Rabbit anti-Pinin	Thermo Scientific	Cat #: 18266-1-AP; RRID:AB_10642138
Rabbit anti-SFPQ	Abcam	Cat #: ab177149
Rabbit anti-ZC3H14 (MSUT2)	Sigma-Aldrich	Cat #: HPA049798; RRID:AB_2680888
Rabbit anti-DDX39B	OriGene	Cat #: TA890032
Rabbit anti-DYRK1A	Abcam	Cat #: ab65220; RRID:AB_1140733
Rabbit anti-SRSF2	Abcam	Cat #: ab204916
Rabbit anti-SNRNP70 (U1-70K)	Abcam	Cat #: ab83306; RRID:AB_10673827
Rabbit anti-PABP	Abcam	Cat #: ab21060; RRID:AB_777008
Rabbit anti-TIA1	Abcam	Cat #: ab40693; RRID:AB_2201438
Rabbit anti-SRRM3	Sigma-Aldrich	Cat #: HPA019337; RRID:AB_1848909
Rabbit anti-SRSF1 (SF2)	Abcam	Cat #: ab129108; RRID:AB_11141636
Mouse anti-G3BP	Abcam	Cat #: ab56574; RRID:AB_941699
Rabbit anti-SNRPA1	Millipore Sigma	Cat #: HPA045622; RRID:AB_2679394
Rabbit anti-PQBP1	Millipore Sigma	Cat #: HPA001880; RRID:AB_1079671
Rabbit anti-PNISR	Millipore Sigma	Cat #: HPA038796; RRID:AB_10672652
Rabbit anti-RPF1	Sigma-Aldrich	Cat #: HPA024642; RRID:AB_1856428
Rabbit anti-U2AF1	Sigma-Aldrich	Cat #: HPA044833; RRID:AB_10960990
Rabbit anti-SON	Thermo Fisher	Cat #: PA565108; RRID:AB_2662628
Mouse anti-SRSF3	Thermo Fisher	Cat #: 7B4A12; RRID:AB_2533119
Rabbit anti-Fibrillarin	Invitrogen	Cat #: MA1-22000; RRID:AB_2231906
Rabbit IgG isotype control antibody	ThermoFisher	Cat #: 10500C; RRID:AB_2532981
Goat anti-mouse 647	Abcam	Cat #: ab150115; RRID:AB_2687948
Goat anti-rabbit 647	Abcam	Cat #: ab150079; RRID:AB_2722623
Goat anti-mouse biotinylated	Vector labs	Cat #: BP-9200; RRID:AB_2827937
Bacterial and virus strains		
pLenti CMV Blast	Campeau et al., 2009	Addgene plasmid #17451; RRID:Addgene_17451
Biological samples		
Human brain samples	Table S3	N/A
Chemicals, peptides, and recombinant proteins		
Sarkosyl	Sigma	Cat #: 61747
Benzonase	Sigma	Cat #: E1014-25KU
Sodium PTA	Sigma	Cat #: P6395
Lipofectamine 2000	ThermoFisher	Cat #: 11668027
Blasticidine S hydrochloride	Sigma	Cat #: 15205-25MG
Triton X-100	Fisher	Cat #: BP151-100

(*Continued on next page*)

Continued

REAGENT or RESOURCE	SOURCE	IDENTIFIER
Deionized formamide	Calbiochem 4610	Cat #: 4610
ProLong Glass Antifade Mountant	ThermoFisher	Cat #: P36980
5-Propargylamino-ddUTP-Cy5	JenaBioscience	Cat #: NU-1619-CY5
RNasein Plus RNase Inhibitor	Promega	Cat #: N2615
Terminal Deoxynucleotidyl Transferase	ThermoFisher	Cat #: EP0161
cOmplete ULTRA Tablets	Sigma	Cat #: 05892791001
PhosSTOP	Sigma	Cat #: 4906837001
RiboLock RNase Inhibitor	ThermoFisher	Cat #: EO0382
Turbo DNase	ThermoFisher	Cat #: AM2239
Proteinase K	ThermoFisher	Cat #: 25-530-049
Guanidine Hydrochloride	Sigma	Cat #: G3272-500G
TrizolLS	ThermoFisher	Cat #: 10296028
Diethyl pyrocarbonate (DEPC)	Sigma	Cat #: D5758-25ML
0.1X citrate buffer	Sigma	Cat #: C9999
FISH Hybridization buffer	Stellaris	Cat #: SMF-HB1-10
Vectashield Vibrance antifade mounting medium	Vector Laboratories	Cat #: H-1700
Scytek SUPER BLOCK	Fisher	Cat #: NC9782835
Avidin/Biotin blocking kit	Vector Labs	Cat #: SP-2001
hematoxylin	Sigma Aldrich	Cat #: H3136
Vectastain Elite ABC reagent	Vector Labs	Cat #: PK-6100
Vector Immpact NovaRED peroxidase substrate kit	Vector Labs	Cat #: SK-4800
Critical commercial assays		
Zymo Oligo Clean and Concentrate spin-column kit	Zymo	Cat #: D4060
QuBit RNA HS Assay kit	ThermoFisher	Cat #: Q328521
Agilent 4200 TapeStation using the High Sensitivity RNA ScreenTape	Agilent	Cat #: 5067-5579
KAPA RNA HyperPrep Kit with RiboErase	Roche	Cat #: KK8560
Nugen Ovation SoLo RNA-Seq System, Mouse	Nugen	Cat #: 0501-32
Dynabeads Protein A for Immunoprecipitation	ThermoFisher	Cat #: 10002D
Deposited data		
RNA sequencing data	This paper	GSE148716
Experimental models: cell lines		
HEK293 tau biosensor cells	ATCC	ATCC Cat# CRL-3275; RRID:CVCL_DA04
H4 cells	ATCC	ATCC Cat# HTB-148; RRID:CVCL_1239
Experimental models: organisms/strains		
P301S mice (Tg2541) B6-Tg(Thy1-MAPT*P301S)2541	Allen et al., 2002	N/A
WT mice (rTg21221) FvBB6F1-Tg (Camk2a-tTa),(tetO-MAPT*wt)21221	Hoover et al., 2010	N/A
P301L mice (rTg4510) FvBB6F1-Tg(Camk2a-tTA)1Mmay, (tet)-tdTomato-Syp/EGFP)1.1Luo/J,(tetO-MAPT*P301L)4510	Ramsden et al., 2005	N/A
Non-transgenic mice (C57BL/6J)	Jackson Laboratory	Stock No. 000664 | B6

(*Continued on next page*)

Please cite this article in press as: Lester et al., Tau aggregates are RNA-protein assemblies that mislocalize multiple nuclear speckle components, Neuron (2021), https://doi.org/10.1016/j.neuron.2021.03.026

Continued

REAGENT or RESOURCE	SOURCE	IDENTIFIER
Oligonucleotides		
sgRNAs for SRRM2_FL-halo. Up: CACCGCCATGAGACAC CGCTCCTCC down: AAACG GAGGAGCGGTGTCTCATGGC	This paper	N/A
sgRNAs for SRRM2_dIDR-halo. Up: CACCGCTGGCATGCCGAGAAACTT down: AAACAAGTTTCTCGGCATGCCAGC	This paper	N/A
Fluorescence *in situ* hybridization probes	Table S6	N/A
Recombinant DNA		
pCRIPaint-HaloTag-PuroR	Schmid-Burgk et al., 2016	Addgene plasmid #80960; RRID:Addgene_80960
PX458-CAS9	Schmid-Burgk et al., 2016	Addgene plasmid #48138; RRID:Addgene_48138
pCAS9-mCherry-Frame_selector +0	Schmid-Burgk et al., 2016	Addgene plasmid #66939; RRID:Addgene_66939
pCAS9-mCherry-Frame_selector +2	Schmid-Burgk et al., 2016	Addgene plasmid #66941; RRID:Addgene_66941
pIRESpuro3	Clontech	Cat: 631619
Software and algorithms		
CellProfiler image analysis software Version 3.1.8	McQuin et al., 2018	https://cellprofiler.org/
Ilastik image segmentation software Version 1.3.3	Berg et al., 2019	https://www.ilastik.org/
MAJIQ splicing analysis software Version 2.1	Vaquero-Garcia et al., 2016	https://majiq.biociphers.org/
STAR RNAseq aligner Version 2.6.0	Dobin et al., 2013	https://github.com/alexdobin/STAR
RepEnrich repetitive element analysis Version 1	Criscione et al., 2014	https://github.com/nskvir/RepEnrich
iREAD intron analysis software Version 0.8.5	Li et al., 2020	https://github.com/genemine/iread
DEseq2 Version 1.30.1	Love et al., 2014	https://bioconductor.org/packages/release/bioc/html/DESeq.html
Trimmomatic Version 0.36	Bolger et al., 2014	http://www.usadellab.org/cms/?page=trimmomatic
FastQ Screen Version 0.12.0	Wingett and Andrews, 2018	https://www.bioinformatics.babraham.ac.uk/projects/fastq_screen/
Prism 9	GraphPad	https://www.graphpad.com/scientific-software/prism/
Other		
Nikon Spinning Disc Confocal microscope	Biofrontiers imaging core	RRID: SCR_018302
Round cover glass, #1.5 thickness	Thomas Scientific	Cat #: 1217N79
NanoDrop OneC UV-Vis Spectrophotometer	ThermoFisher	Cat #: 840-274200
245 mm square tissue culture treated dishes	Corning	Cat #: 07-200-599
Evos Imaging system	Evos	Cat #: M500
BD Biosciences FACSAria Fusion flow cytometer	BIofrontiers flow cytometry core	RRID:SCR_019309
Illumina NextSeq	Biofrontiers sequencing core	RRID: SCR_019308
Optima MAX-XP ultracentrifuge	Beckman Coulter	Cat #: 393315
Ultracentrifuge tubes	Beckman Coulter	Cat #: 349623

Please cite this article in press as: Lester et al., Tau aggregates are RNA-protein assemblies that mislocalize multiple nuclear speckle components, Neuron (2021), https://doi.org/10.1016/j.neuron.2021.03.026

RESOURCE AVAILABILITY

Lead contact

Further information and requests for resources and reagents should be directed to and will be fulfilled by the Lead Contact, Roy Parker (Roy.Parker@Colorado.edu)

Materials availability

All unique/stable reagents generated in this study are available from the Lead Contact without restriction.

Data and code availability

The accession number for the RNA sequencing data reported in this paper is GEO: GSE148716.

EXPERIMENTAL MODEL AND SUBJECT DETAILS

Tauopathy mouse models

Animals were maintained in a facility accredited by the Association for Assessment and Accreditation of Laboratory Animal Care in accord with the Guide for the Care and Use of Laboratory Animals. All procedures were approved by the University of California, San Francisco, Institutional Animal Care and Use Committee. Animals were maintained under standard environmental conditions, with a cycle of 12 hours light and 12 hours dark and free access to food and water.

For tau seeding experiments in HEK293 tau biosensor cells, the following mice were used: homozygous B6-Tg(Thy1-MAPT*P301S) 2541 mice (referred to as Tg2541 or P301S tau mice in cellular seeding experiments) and FvBB6F1-Tg(Camk2a-tTa),(tetO-MAPT*wt) 21221 (referred to as rTg21221 or WT tau mice in cellular seeding experiments). Mice were euthanized when the P301S tau mice developed spontaneous pathology (6-7 months). Collected brains were homogenized to 10% (wt/vol) in DPBS, aliquoted, and frozen at −80°C.

For tau isolation and sequencing of tau aggregates, the following mice were used: FvBB6F1-Tg(Camk2a-tTA)1Mmay, (tet)-tdTomato-Syp/EGFP)1.1Luo/J,(tetO-MAPT*P301L)4510 (referred to as rTg4510 or P301L mice in sequencing experiments) and FvBB6F1-Tg(Camk2a-tTa),(tetO-MAPT*wt)21221 (referred to as rTg21221 or WT tau mice in sequencing experiments). An even split of male and female mice were used and we did not observe any influence or associaition of sex on the findings.

For IF and FISH experiments, the following mice were used: homozygous B6-Tg(Thy1-MAPT*P301S)2541 mice (referred to as Tg2541 or P301S tau mice in IF and FISH experiments) and C57BL/B6 non transgenic mice (referred to as WT in IF and FISH experiments) were used as a control.

Cell culture and tau seeding of H4 biosensor cells

H4 cells (ATCC Cat# HTB-148, RRID:CVCL_1239) stably expressing the *pIRESpuro3* vector (Clontech) containing a codon-optimized 0N4R MAPT gene with the P301S point mutation and tagged with YFP were cultured in Dulbecco's Modified Eagle's Medium (DMEM) supplemented with 10% fetal bovine serum (FBS) and 0.2% penicillin-streptomycin, and maintained in incubators set to 37°C with 5% carbon dioxide. Cells were plated in a 12-well glass-bottomed dish at $1x10^5$ cells/well and allowed to settle for a minimum of 2 hours prior to infection with PTA-precipitated tau prions from Tg2541 mouse brain.

Cell culture and tau seeding in HEK293 biosensor cells

HEK293 tau biosensor cells stably expressing the 4R RD of tau with the P301S mutation were purchased from ATCC (ATCC Cat# CRL-3275, RRID:CVCL_DA04) (previously described in Holmes et al., 2014). Cells were seeded at 2.5×10^5 cells/mL in 500uL of DMEM with 10% FBS and 0.2% penicillin-streptomycin antibiotics on PDL coated glass coverslips in a 24-well tissue culture treated plate (Corning 3526) and allowed to grow overnight in incubators set to 37°C with 5% carbon dioxide. The next day, 7ug of 1 mg/mL clarified P301L tau or WT tau mouse brain homogenate was mixed with 6uL of Lipofectamine 2000 and brought up to 100uL in PBS and allowed to sit at room temperature for 1.5 hours. The mixture was then added to 300uL of DMEM without FBS or antibiotics and mixed by pipetting. 50uL of this mixture was added to each well of a 24 well plate and allowed to incubate at 37°C for 24 hours. Tau aggregate formation was monitored using a fluorescence microscope with a 488nm filter.

METHOD DETAILS

Clarification of brain homogenate for tau aggregate seeding in HEK293 cells

10% brain homogenate from Tg2541 or WT mice was centrifuged at 500 x g for 5 minutes, the supernatant was transferred to a new tube and centrifuged again at 1,000 x g for 5 minutes. The supernatant was again transferred to a new tube and the protein concentration was measured using bicinchoninic acid assay (BCA), and diluted in DPBS to 1 mg/mL for transfection into HEK293 tau biosensor cells.

Please cite this article in press as: Lester et al., Tau aggregates are RNA-protein assemblies that mislocalize multiple nuclear speckle components, Neuron (2021), https://doi.org/10.1016/j.neuron.2021.03.026

PTA precipitation from brain homogenate for tau aggregate seeding in H4 biosensor cells

PTA precipitation of tau aggregates from mouse brain was performed as described (Woerman et al., 2016). 10% brain homogenate was incubated in final concentrations of 2% sarkosyl (Sigma, 61747) and 0.5% benzonase (Sigma, E1014-25KU) with constant agitation at 37°C for 2 hours. Sodium PTA (Sigma, P6395) was made in ultrapure MilliQ H_2O and the pH was adjusted to 7.0. PTA was added to the samples to a final concentration of 2%, and samples were then incubated shaking at 37°C overnight. The samples were centrifuged at 13,200 × g at room temperature for 30 minutes, and the supernatant was removed. The resulting pellet was resuspended in 2% sarkosyl/PBS and 2% PTA. The sample was again incubated shaking at 37°C for 2 hours before a second centrifugation as above. The supernatant was again removed, and the pellet was resuspended in 1X PBS to 10% of the initial starting volume. This suspension was incubated using 1 μL/well with Lipofectamine 2000 and OptiMEM at room temperature for at least 1.5 hours prior to infecting cells.

Fluorescent labeling of oligonucleotides for FISH

As previously described (Gaspar et al., 2017), DNA oligonucleotides were labeled with ddUTP-Cy5 fluorophores using terminal deoxynucleotidyl transferase (TdT). DNA oligonucleotides were designed to be antisense to the target of interested with the following specifications: 18-22 nucleotides in length and a minimum of 2 nucleotide spacing between probes. 20uM of DNA oligonucleotides were mixed with 120uM of 5-Propargylamino-ddUTP-Cy5, 10 units of TdT, and 1X TdT buffer and incubated at 37°C for 16 hours. Following incubation, oligonucleotides were precipitated in 80% ethanol with 60mM Na-acetate at −80°C for 20 minutes. The oligonucleotides were pelleted by centrifugation at 16,000 g for 20 minutes at 4°C, washed with 80% ethanol 2x, air-dried, and brought up in 20uL of nuclease free H20. If necessary, a further round of purification can be performed with the Zymo Oligo Clean and Concentrate spin-column kit (Zymo D4060). Labeled probe concentration was measured via NanoDrop OneC UV-Vis Spectrophotometer (Thermo Scientific 840-274200).

Tau aggregate isolation from HEK293 cells via centrifugation and flow cytometry

HEK293 biosensor cells were grown to 70%–80% confluency in 245 mm square tissue culture treated dishes (Corning 07-200-599) in 50mL of DMEM (one plate per biologic replicate). 200 ug of WT or P301S tau clarified mouse brain homogenate was transfected per dish using lipofectamine 2000 and incubated at 37°C for 24 hours. Tau aggregation was monitored using the Evos M500 Imaging System with a GFP filter. Cells were harvested by scraping, centrifuged at 200 *rcf.*, snap frozen in liquid nitrogen, and stored at −80°C.

The cell pellet was thawed on ice for 5 minutes and resuspended in 6mL of high salt, high sucrose buffer containing RNase Inhibitors (10mM Tris-HCl pH 7.4, 0.8M NaCl, 1 mM EGTA, 10% sucrose, 0.5% NP40, Complete ultra-protease inhibitor, PhosStop Phosphatase inhibitor, 1:1500 RNasein, 1:300 Ribolock, 1:60 turbo DNase). Cell lysate was passed through a 25 G needle 3x to homogenize and 100uL of sample was taken to extract total RNA.

Large tau complexes were pelleted by centrifugation at 21,000 g for 20 minutes at 4°C, the pellet was brought up in high salt/high sucrose buffer, passed through a 27G needle, and centrifuged at 10,000 g for 10 minutes at 4°C. The pellet was brought up in 1mL of DPBS and centrifuged at 500 g for 5 minutes at 4°C to pellet large cellular debris. The supernatant (S3, enriched tau fraction) was taken and spotted onto a microscope slide for fluorescent imaging of tau aggregates in solution.

A BD Biosciences FACSAria Fusion flow cytometer (RRID:SCR_019309) was used to sort tau aggregates by fluorescence and size. The sheath fluid was changed to PBS, flow rate was set to 1.2, and threshold rate was set to < 200 events/second. Gates were set on side scatter-H and 488 fluorescence such that WT transfected S3 fractions had < 1% of particles in sorted fraction and P301S transfected S3 fractions had > 30% in the sorted fraction. Roughly 1 million particles were sorted for each sample. To ensure the flow cytometer was sorting particles properly, the sorted fraction was visually inspected by fluorescence microscopy and the sorted and waste fractions were run back through the flow cytometer.

To denature tau aggregates and extract RNA, the sorted fractions were brought up in Proteinase K buffer (2M Urea, 100ug/mL proteinase K, and 3mM DTT) and incubated at room temperature for 15 minutes. Guanidine Hydrochloride was added to a final concentration of 5M and incubated at room temperature for 30 minutes. RNA was then extracted with TRIzol LS reagent (ThermoFisher 10296010). RNA concentrations were measured by QuBit RNA HS Assay kit (ThermoFisher Q328521) and Agilent 4200 TapeStation using the High Sensitivity RNA ScreenTape (Agilent 5067-5579). All samples except for the WT transfected sorted fraction yielded sufficient RNA to prepare sequencing libraries. RNA sequencing libraries were then prepared from total RNA and tau aggregate associated RNA from HEK293 biosensor cells using the Roche KAPA RNA HyperPrep Kit with RiboErase (Kapa KK8560) and sequenced on an Illumina NextSeq sequencer at the University of Colorado, Boulder BioFrontiers Sequencing Core (RRID: SCR_019308).

Isolation of tau aggregates from mouse brain

Brains were harvested from two Tg21221 (WT 0N4R human tau mouse brains) and two rTg4510 (P301L 0N4R human tau) mice and snap frozen in liquid nitrogen. Samples were thawed on ice and weighed. The brain tissue was then homogenized on ice using a dounce homogenizer and diluted to 5 mL/g in homogenization buffer with RNase inhibitors (10mM Tris-HCl pH7.4, 0.8M NaCl, 1mM EGTA, 10% sucrose, 1X Roche protease inhibitor, 1:40 promega RNasein). Aliquots were stored at −80 C.

To extract total RNA, 50uL of brain homogenate was incubated for 2 hours at room temperature in proteinase K buffer (2% SDS, 4M Urea, 10mM Tris-HCl pH4.54, 100ug/mL Proteinase K). 400uL of Urea buffer (60mM Tris-HCl pH 8.5, 8M Urea, 2% SDS) was then

Please cite this article in press as: Lester et al., Tau aggregates are RNA-protein assemblies that mislocalize multiple nuclear speckle components, Neuron (2021), https://doi.org/10.1016/j.neuron.2021.03.026

added and incubated for 30 minutes at room temperature. RNA was extracted from one half of this reaction using TRIzol LS solution and the other half was frozen at −80°C.

900uL of frozen brain homogenate was thawed on ice and 100uL of 10% (w/v) sarkosyl solution was added and incubated on ice for 15 minutes. Homogenate was then passed through a 25G and 27G syringe. Protein concentrations were measured by QuBit Protein Assay Kit (Thermo Fisher, Q33211) and sarkosyl buffer (50mM HEPES pH 7.2, 250 mM sucrose, 1mM EDTA, 1% w/v sarkosyl, 0.5 M NaCl) was added to reach a final concentration of 10 mg/mL. 500uL of each sample was transferred into an ultracentrifuge tube (Beckman Coulter, 349623) and centrifuged at 180,000 g for 30 min at 4 deg in a Beckman Coulter Optima MAX-XP Ultracentrifuge. The supernatant (S1 fraction) was removed and stored at −80°C. The pellet was then brought up in 500uL of sarkosyl buffer and run through a 25G needle to homogenize. The sample was then centrifuged at 180,000 g for 30 min at 4°C and the supernatant (S2) was removed and stored at −80°C.

For the sarkosyl insoluble RNA sequencing, P2 pellet was brought up in 100uL of proteinase K buffer and incubated at RT for 2 hours at RT. To further solubilize the sample, 400uL of urea buffer was added and incubated at RT for 30 minutes. The sample was then split in two and RNA was extracted from one half (250uL) using Trizol LS solution the other half was frozen at −80°C.

For the Tau IP, the P2 fraction was brought up in 400uL of PBS and protein concentrations were measured using the QuBit Protein Assay Kit (Thermo Fisher, Q33211). Samples were precleared with 15mg of DEPC treated (to inactivate RNase) protein A dynabeads at room temperature for 45 minutes at RT on rotator. While preclearing, Tau12 and IgG antibodies were conjugated to 50uL (1.5mg) of protein A dynabeads for 40 minutes on rotator. Following preclear step, the sample was split into two fractions (one for the Tau12 IP and one for the IgG IP). Dynabeads with conjugated antibody were washed with PBS, brought up in 50uL of PBS and added to sample. IP was carried out on rotator at room temperature for 40 minutes. Sample was then washed 3x with PBS and 100uL of proteinase K buffer was added to the beads and incubated at RT for 2 hours. 400uL of urea buffer was added to beads and incubated for 30 minutes to further denature. Samples were then split into two 250uL fractions, one was Trizol extracted. RNA concentrations were then measured by QuBit RNA HS Assay kit (ThermoFisher Q328521) and Agilent 4200 TapeStation using the High Sensitivity RNA ScreenTape (Agilent 5067-5579). IgG IP did not pull down any RNA. RNA sequencing libraries were prepared using the Nugen Ovation SoLo RNA-Seq System, Mouse (Nugen 0501-32) and sequenced on an Illumina NovaSeq sequencer at the University of Colorado, Anschutz Genomics and Microarray Core.

Generation of Lentiviral particles

As previously described (Burke et al., 2019), HEK293T cells (T25 Flask at 80% confluence) were co-transfected with 1ug of pLenti-SRSF2-mCherry-blasticydin, 1ug of pVSV-G, 1ug of pRSV-Rev, and 1ug of pMDLg-pRRe using 16uL of lipofectamine 2000. Medium was replaced 6 hours post-transfection. Medium was then collected at 24- and 48-hours post-transfection and filter sterilized with a 0.45-um filter.

Generating SRSF2-mCherry cells via lenti-virus

HEK293 biosensor cells were seeded in a T-25 flask. When 80% confluent, the cells were incubated for 1 hour with 1mL of SRSF2-mCherry-blasticydin lentiviral particles containing 10-ug of polybrene with periodic rocking. 4mL of normal medium was then added to the flask and incubated for 24 hours. Normal medium was then aspirated and replaced with selective medium containing 10-ug/mL of Blasticidine S hydrochloride (Sigma-Aldrich). Selective medium was changed every three days. After one-week, selective medium was replaced with normal growth medium. Expression of SRSF2-mCherry was confirmed by fluorescence microscopy.

Generating halo tagged SRRM2 cells using CRISPaint

HEK293 biosensor cells were seeded in a 6 well plate. As previously described (Ilik et al., 2020; Schmid-Burgk et al., 2016) when 80% confluent, cells were transfected with 1 ug of pCRIPaint-HaloTag-PuroR plasmid (RRID:Addgene_80960)), 0.5 ug of PX458-CAS9 targeting plasmid (RRID:Addgene_48138), 0.5 ug of pCAS9-mCherry-Frame_selector plasmid (either RRID:Addgene_66939 for SRRM2_FL-Halo or RRID:Addgene_66941 for SRRM2_dIDR-Halo). After 24 hours, cells were selected using 2 ug/mL puromycin for 48 hours to enrich for edited cells. To label the halo constructs, JF646 was added to growth media at 10 nM overnight prior to cell lysis for gel analysis or fixation for imaging. CRISPR targeting guide sequences for SRRM2_FL-halo: CACCGCCATGAGAC ACCGCTCCTCC and AAACGGAGGAGCGGTGTCTCATGGC and SRRM2_dIDR-halo: CACCGCTGGCATGCCGAGAAACTT and AAACAAGTTTCTCGGCATGCCAGC

Immunofluorescence (IF) in HEK293 and H4 cells

Cells were fixed in 4% FPA for 10 minutes, washed 3X with DPBS, permeabilized in 0.1% Triton X-100 (Fisher BP151-100) for 5 minutes, washed 3x with PBS, and blocked with 5% bovine serum albumin (BSA) for 1 hour. Primary antibodies were diluted to desired concentration in 5% BSA and incubated overnight at 4 deg. Slides were washed 3x with DPBS and secondary antibodies were added at appropriate dilution in 5% BSA and allowed to incubate at room temperature for 1 hour. Slides were washed 2x with DPBS and then incubated in DAPI diluted in PBS (1ug/mL) for 5 minutes at RT, washed 1X with DPBS and then mounted on microscope slides with Prolong glass antifade mountant.

Please cite this article in press as: Lester et al., Tau aggregates are RNA-protein assemblies that mislocalize multiple nuclear speckle components, Neuron (2021), https://doi.org/10.1016/j.neuron.2021.03.026

Fluorescence *in situ* hybridization (FISH)

As previously described (Khong et al., 2017), cells were fixed in 4% PFA for 10 minutes, washed 3x with PBS, permeabilized in 70% ethanol for 1 hour at 4°Cells were then incubated in a wash buffer consisting of 2X nuclease free SSC and 10% deionized formamide (Calbiochem 4610) for 5 minutes at room temperature. The FISH probes were diluted to desired concentration in 100uL of hybridization buffer (2X nuclease-free SSC, 10% deionized formamide, 10% dextran sulfate) and spotted onto parafilm in a hybridization chamber (10cm cell culture dish lined with wet paper towels and covered with parafilm). Coverslips were then inverted onto the droplet of hybridization buffer contain the FISH probes and incubated at 37°C overnight. The slides were then transferred back to a 24 well plate and 500uL of 2X nuclease free SSC with 10% deionized formamide was added for 30 minutes at 37°C. Cells were then incubated in DPBS with 1ug/mL DAPI at room temperature for 5 minutes, washed with 2X nuclease free SSC and incubated at room temperature for 5 minutes. Coverslips were mounted on microscope slides with ProLong Glass Antifade Mountant (ThermoFisher, P36980) and allowed to cure overnight at room temperature. minutes.

Fluorescence recovery after photobleaching

HEK293 biosensor cells were seeded in DMEM supplemented with 10% FBS and 0.2% penicillin-streptomycin at 0.25x10^5 cells/mL in Grenier Bio-One CELLview dishes with Glass Bottoms (Thomas Scientific, 07-000-235) and grown overnight at 37°C. The next day, clarified P301S tau brain homogenate was transfected and grown for 24 hours. A Nikon A1R Laser Scanning Confocal with environmental chamber was used to image the cells. A circular region within a tau aggregate was defined and bleached using a 405nm laser set to 100% laser power. For determining the recovery of tau within tau aggregates (Figures S1B and S1C), fluorescence intensity was measured continuously for 6 minutes and 30 s post bleaching and normalized to an unbleached region (N = 5). For determining the recovery of SRRM2_FL-halo within splicing speckles with and without tau aggregates, fluorescence intensity was measured continuously for 30 s and normalized to an unbleached region (n = 5) (Figure 6A). For determining the recovery of SRSF2-mCherry within splicing speckles with and without tau aggregates, fluorescence intensity was measured every 1 s for 30 s and normalized to an unbleached region (n = 5) (Figure 6B).

Mouse brain RNA fluorescent *in situ* hybridization followed by immunofluorescent staining (RNA FISH-IF)

Control (B6/J) and Tg2541 animals at approximately 6 months of age were anesthetized for whole brain collection. The mouse brains were embedded in OCT compound (Sakura, 4583) and flash-frozen in chilled isopentane. Samples were sectioned at 12 μm using a cryostat and mounted on glass slides. Samples were air-dried at room temperature for 20 minutes to ensure tissue adherence to slides, then fixed in cold 4% PFA/1X PBS for 15 minutes. Samples were washed 3 times in 1X PBS for 5 minutes/wash, followed by a wash in 1X SSC for 5 minutes. Samples were transferred into 0.1X citrate buffer (Sigma, C9999) for a gentle antigen retrieval at 60°C for 1 hour 15 minutes. The slides were allowed to cool for 15 minutes, then rinsed 3 times in 1X SSC for 5 minutes/wash. Samples were then dehydrated in a graded series of ethanol washes (50%, 70%, 90% and 100%) for 3 minutes/wash and air-dried for 10 minutes. A hydrophobic barrier was drawn around the tissue and samples were blocked in a pre-hybridization buffer of 3% normal goat serum (NGS)/4X SSC at 37°C for 1 hour in a humidified chamber. Oligo(dT) probe labeled with Quasar 570 or Quasar 670 (Stellaris) was added to hybridization buffer (Stellaris, SMF-HB1-10) and incubated at 65°C for 10 minutes followed by a cooling on ice for 2 minutes. Pre-hybridization buffer was removed, and samples were then incubated in probe/hybridization buffer at 37°C overnight.

The next day, samples were washed in a dilution series of pre-hybridization buffer (twice in 4X, then once in 2X, 1X, 0.1X) at 37°C for 10 minutes/wash. Samples were then blocked in 20% NGS/1X PBST (0.1% Tween-20) at room temperature for 1 hour and incubated at room temperature overnight in primary antibodies diluted at 1:250 in 10% NGS/1X PBST.

The next day, samples were washed 3 times in 1X PBST for 10 minutes/wash, then incubated in Alexa Fluor secondary antibodies diluted at 1:500 in 10% NGS/1X PBST for 2 hours at room temperature. Samples were washed 3 times in 1X PBST for 10 minutes/wash. To quench autofluorescence, samples were incubated in 0.1% Sudan Black B in 70% ethanol for 10 minutes, then rinsed briefly in fresh 70% ethanol and transferred into 1X PBS for 5 minutes. Coverslips were mounted onto the slides using Vectashield Vibrance antifade mounting medium with DAPI (Vector Laboratories H-1800) and slides were left to dry overnight prior to being imaged with a Leica SP8 confocal microscope.

Human brain immunofluorescent staining

Human brain samples were provided by the Neurodegenerative Disease Brain Bank at the University of California, San Francisco, which receives funding support from NIH grants P01AG019724 and P50AG023501, the Consortium for Frontotemporal Dementia Research, and the Tau Consortium.

Formalin-fixed paraffin-embedded (FFPE) human brain samples from the left angular gyrus region of control individuals and patients diagnosed with corticobasal degeneration (CBD) were sliced at 8 μm and mounted on glass slides. Samples were deparaffinized in a 60°C oven overnight, followed by two 10-minute xylene washes. Samples were then rehydrated in a graded series of ethanol washes (twice in 100% then once each in 90%, 70%, 50%) for 3 minutes/wash. Slides were then rinsed in cold ultrapure MilliQ H_2O and transferred into 0.1X citrate buffer (Sigma, C9999) for antigen retrieval in an autoclave at 120°C for 5 minutes. Slides were allowed to cool for 15 minutes, then rinsed in 1X PBST (0.25% Triton X-100) for 15 minutes. A hydrophobic barrier was drawn around the tissue and samples were blocked in 20% normal goat serum (NGS)/1X PBST at room temperature for

1 hour in a humidified chamber. Samples were incubated at room temperature overnight in primary antibodies diluted at 1:250 in 10% NGS/1X PBST.

The next day, samples were washed 3 times in 1X PBST for 10 minutes/wash, then incubated in Alexa Fluor secondary antibodies diluted at 1:500 in 10% NGS/1X PBST for 2 hours at room temperature. Samples were washed 3 times in 1X PBST for 10 minutes/wash. To quench autofluorescence, samples were incubated in 0.1% Sudan Black B in 70% ethanol for 10 minutes, then rinsed briefly in fresh 70% ethanol and transferred into 1X PBS for 5 minutes. Samples were incubated for 10 minutes in 5 μg/mL DAPI diluted in 1X PBS, then washed for 10 minutes in 1X PBS. Coverslips were mounted onto the slides using Vectashield Vibrance anti-fade mounting medium (Vector Laboratories H-1700) and slides were left to dry overnight prior to being imaged with a Leica SP8 confocal microscope.

Human tissue samples for immunohistochemistry

AD, FTD and non-neurologic disease control post-mortem tissue samples were obtained from the University of Pittsburgh ALS Tissue Bank, the Barrow Neurological Institute ALS Tissue Bank, and the Target ALS Human Postmortem Tissue Core. All tissues samples were collected after informed consent from the subjects or by the subjects' next of kin, complying with all relevant ethical regulations. The protocol and consent process were approved by the University of Pittsburgh Institutional Review Board (IRB) and the Dignity Health Institutional Review Board. Clinical diagnoses were made by board certified neuropathologists. Subject demographics are listed in Table S3.

Immunohistochemistry

Paraffin-embedded post-mortem frontal cortex tissue sections were used for this study. All sections were deparaffinized, rehydrated and antigen retrieval performed using Target Antigen Retrieval Solution, pH 9.0 (DAKO) for 20 min in a steamer. After cooling to room temperature, non-specific binding sites were blocked using Super Block (Scytek), supplemented with Avidin (Vector Labs). Primary antibodies used for immunohistochemistry were incubated overnight in Super Block with Biotin. Slides were then washed and incubated for 1 h in the appropriate biotinylated IgG secondary antibodies (1:200; Vector Labs) in Super Block. Slides were washed in PBS and immunostaining visualized using the Vectastain Elite ABC reagent (Vector Labs) and Vector Immpact NovaRED peroxidase substrate kit (Vector Labs). Slides were counterstained with hematoxylin (Sigma Aldrich) and pictures were captured using an OLYMPUS BX40 microscope equipped with a SebaCam camera.

QUANTIFICATION AND STATISTICAL ANALYSIS

Information on the statistical analysis and software used can be found in this section and in the Key resources table, statistical details of experiments can be found in the figure legends (including statistical tests used, value of n, what n represents, definition of center, and dispersion and precision measures). D'Agostino-Pearson was used check for normality. Normally distributed data was tested for significance using an un-paired two-tailed t test, non-normally distributed data was analyzed using a Mann-Whitney test. All statistical analyses were performed using Prism version 9 unless otherwise mentioned.

Image analysis

To quantify FISH intensity within nuclear and cytosolic tau aggregates, ImageJ's freehand selection tool was used to draw perimeters around aggregates and in regions of bulk cytosol and nucleus. The average FISH intensity was measured within the selections and used to compare enrichment of RNAs.

To quantify the percentage of SRRM2 in the cytosol of cells, CellProfiler was used. Nuclei were identified using object detection with a typical diameter between 50-200 pixels for HEK293 and H4 cells, which were then used as a mask to quantify nuclear and cytosolic SRRM2 intensity. The percentage of total SRRM2 intensity in the cytosol was calculated by dividing the cytosolic SRRM2 intensity by the sum of the nuclear and cytosolic intensities per image. Significance we determined using an unpaired two-tailed t test.

To quantify enrichment scores of various proteins of interest (POIs) in tau aggregates, 25 images were taken in a 5x5 panel of each slide using a 40x air objective on a Nikon Spinning Disc Confocal microscope (RRID: SCR_018302). Ilastik was used to create the following segmentation masks: cytosolic tau aggregates, nuclear tau aggregates, nucleus, cytosol, and background. The RGB images and segmentation masks were fed into CellProfiler, which was used to quantify the average POI intensity within tau aggregates and the average POI intensity within the corresponding compartment. Enrichment was defined as the ratio of POI intensity within the tau aggregate to the POI intensity within the corresponding compartment.

Analysis of RNA sequencing data

Following sequencing, quality of sequencing reads were assessed using FASTQC version 0.11.5, Illumina TruSeq3 adapters and low quality reads were trimmed off using Trimmomatic version 0.36 (Bolger et al., 2014). Reads that aligned uniquely to the ribosome, yeast, or bacteria were then filtered out using FastQ Screen (Wingett and Andrews, 2018). Reads were aligned using the Spliced Transcripts Alignment to a Reference (STAR) aligner version 2.6.0 (Dobin et al., 2013) to either the Genome Reference Consortium Human Build 38 (GRCh38, acquired from NCBI) or the Genome Reference Consortium Mouse Build 38 (GRCm38, acquired from NCBI)

Please cite this article in press as: Lester et al., Tau aggregates are RNA-protein assemblies that mislocalize multiple nuclear speckle components, Neuron (2021), https://doi.org/10.1016/j.neuron.2021.03.026

depending on the species being analyzed. Adjusted p values were calculated from raw read counts using DEseq2. Gene counts were used to calculate Fragments per kilobase per million read (FPKM) using transcript lengths retrieved from the Ensembl Biomart (Kinsella et al., 2011) and the following formula FPKM = (# of mapped fragments*10^3*10^6)/(transcript length in bp * total number of mapped fragments). For mouse sequencing, FPKM values were used to calculate enrichment scores for each biological replicate (n = 2) by dividing the Tau IP FPKM by the Total RNA FPKM for each replicate. Enrichment scores were then used to calculate average enrichment score for each gene and fold changes between P301L and WT mice. Gene type enrichment was determined by calculating the percentage of FPKM made up by each gene type. Repetitve elements were analyzed using a reference files acquired from repeatmasker (hg38 - Dec 2013 -RepeatMasker open-4.05 – Repeat Library 20140131) and RepEnrich (Criscione et al., 2014).

Splicing analysis: Following mapping of reads to GRCh38 using STAR, MAJIQ v2.1 was used with standard settings to quantify splicing changes. Voila was used to view results, generate splicing diagrams, and determine the relative percentage of each splicing type (only LSVs containing more than 10 reads were reported). To quantify reads mapping to introns, iREAD v0.8.5 was used along with an intron annotation file generated from ensemble v77 (Li et al., 2020). The read count output from iREAD was used as an input to DEseq2 for calling differential intron retention (Love et al., 2014).

Neuron, Volume *109*

Supplemental information

Tau aggregates are RNA-protein assemblies that mislocalize multiple nuclear speckle components

Evan Lester, Felicia K. Ooi, Nadine Bakkar, Jacob Ayers, Amanda L. Woerman, Joshua Wheeler, Robert Bowser, George A. Carlson, Stanley B. Prusiner, and Roy Parker

Figure S1

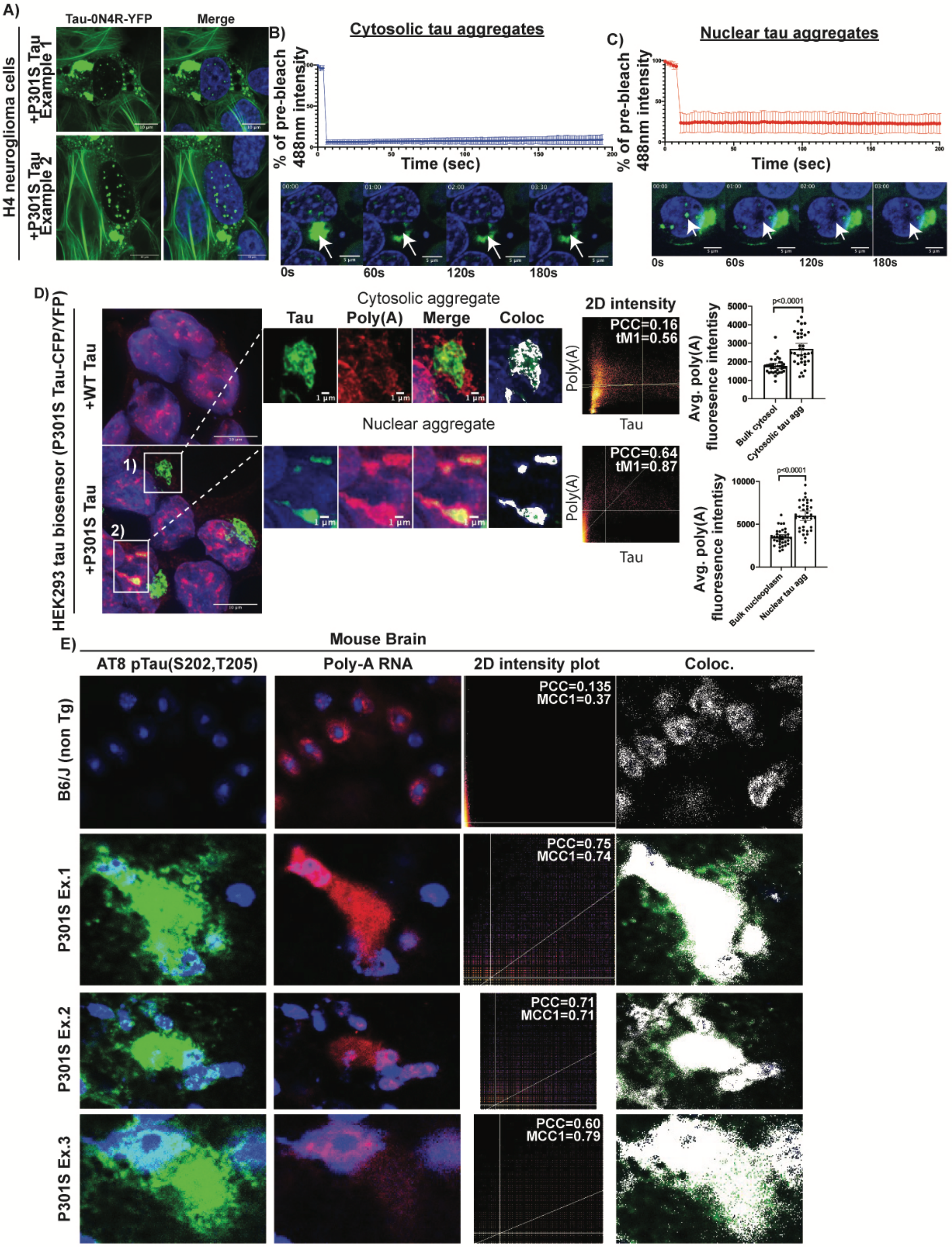
A)
Tau-0N4R-YFP
Merge
H4 neuroglioma cells
+P301S Tau Example 1
+P301S Tau Example 2
B)
Cytosolic tau aggregates
% of pre-bleach 488nm intensity
Time (sec)
0s
60s
120s
180s
C)
Nuclear tau aggregates
% of pre-bleach 488nm intensity
Time (sec)
0s
60s
120s
180s
D)
HEK293 tau biosensor (P301S Tau-CFP/YFP)
+WT Tau
+P301S Tau
1)
2)
Cytosolic aggregate
Tau
Poly(A)
Merge
Coloc
Nuclear aggregate
2D intensity
PCC=0.16
tM1=0.56
PCC=0.64
tM1=0.87
Poly(A)
Tau
Avg. poly(A) fluoresence intentisy
p<0.0001
Bulk cytosol
Cytosolic tau agg
Bulk nucleoplasm
Nuclear tau agg
E)
Mouse Brain
AT8 pTau(S202,T205)
Poly-A RNA
2D intensity plot
Coloc.
B6/J (non Tg)
P301S Ex.1
P301S Ex.2
P301S Ex.3
PCC=0.135
MCC1=0.37
PCC=0.75
MCC1=0.74
PCC=0.71
MCC1=0.71
PCC=0.60
MCC1=0.79

Supplemental figure 1: FRAP of tau aggregates in HEK293 tau biosensor cells and additional examples of tau aggregates containing poly(A) RNA, related to figure 1. (A) H4 neuroglioma cells expressing 0N4R tau-YFP that contain nuclear tau aggregates. See Video S2 for 3D rotation of z-stack showing that the tau aggregates are within the nucleus. **(B, C)** FRAP of nuclear and cytosolic tau aggregates in HEK293 cells. 405 nm laser was used to photobleach and fluorescence intensity was measured in the 488cm channel. Arrow in example images shows bleached area. Data are represented as mean ± standard deviation (n=5). **(D)** FISH for poly(A) RNA in HEK293 cell nuclear and cytosolic tau aggregates**.** Bar graphs show quantification of poly(A) RNA fluorescence intensity within nuclear and cytosolic tau aggregates in relation to bulk cytosol and nucleoplasm. White pixels in Coloc image show pixels above the Costes determined thresholds in 2D intensity plots (PCC = Pearson correlation coefficient and tM1= thresholded manders colocalization (% of tau pixels above threshold that colocalize with poly(A) pixels above threshold)). Data are represented as mean ± 95% confidence intervals and significance was determined using an unpaired two-tailed t-test (n = 35 aggregates). **(E)** Additional examples from B6 non transgenic and P301S mice (Tg2541) showing cytosolic tau aggregates (Ex. 1) and nuclear tau aggregates (Ex. 2, 3) contain RNA.

Figure S2

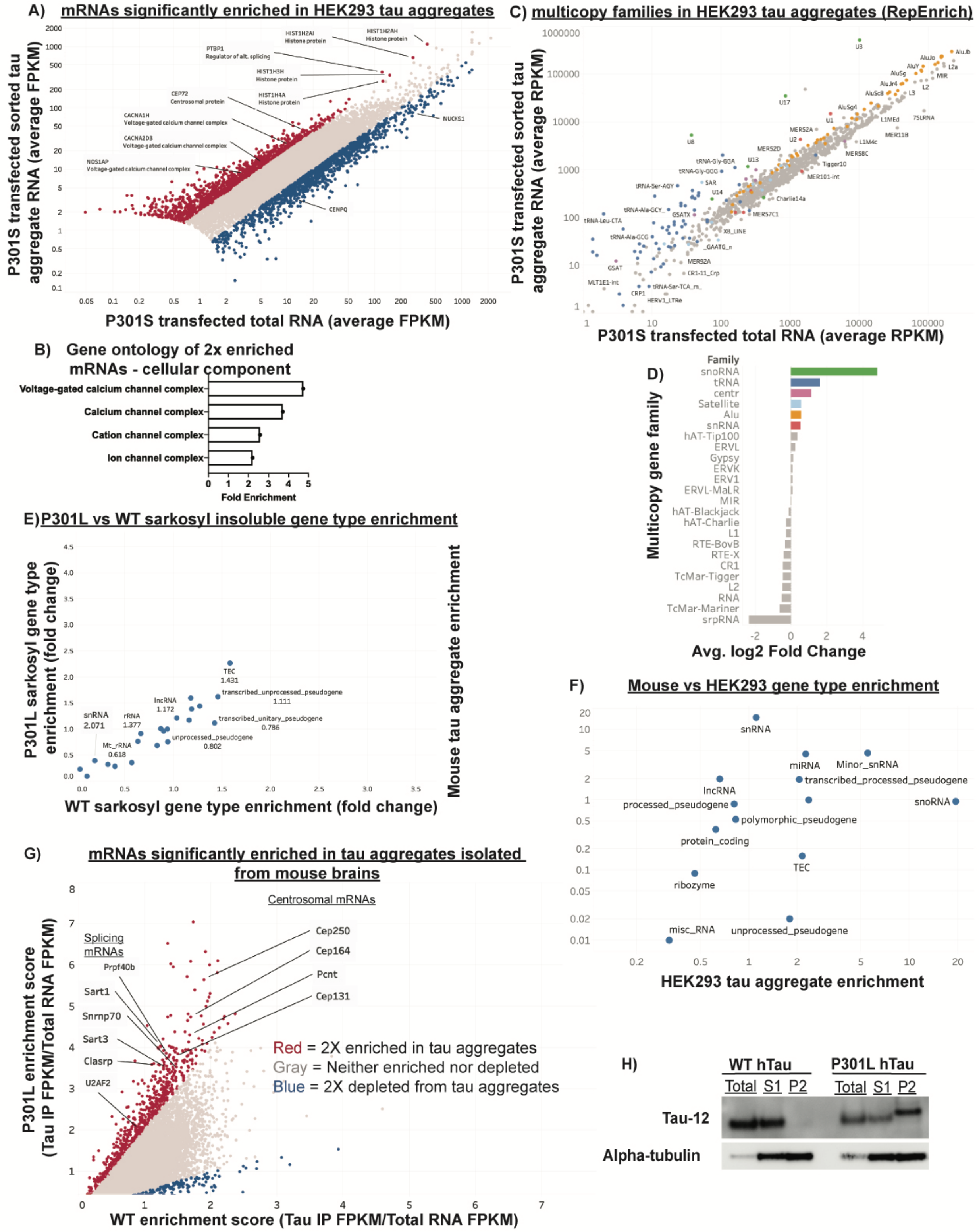
A) mRNAs significantly enriched in HEK293 tau aggregates
P301S transfected sorted tau aggregate RNA (average FPKM)
P301S transfected total RNA (average FPKM)
2000
1000
500
200
100
50
20
10
5
2
1
0.5
0.2
0.1
0.05
0.1
0.2
0.5
1
2
5
10
20
50
100
200
500
1000
2000
HIST1H2AI Histone protein
HIST1H2AH Histone protein
PTBP1 Regulator of alt. splicing
HIST1H3H Histone protein
HIST1H4A Histone protein
CEP72 Centrosomal protein
CACNA1H Voltage-gated calcium channel complex
CACNA2D3 Voltage-gated calcium channel complex
NOS1AP Voltage-gated calcium channel complex
NUCKS1
CENPQ
B) Gene ontology of 2x enriched mRNAs - cellular component
Voltage-gated calcium channel complex
Calcium channel complex
Cation channel complex
Ion channel complex
0
1
2
3
4
5
Fold Enrichment
C) multicopy families in HEK293 tau aggregates (RepEnrich)
P301S transfected sorted tau aggregate RNA (average RPKM)
P301S transfected total RNA (average RPKM)
1000000
100000
10000
1000
100
10
1
1
10
100
1000
10000
100000
U3
AluJb
AluJo
L2a
AluY
AluSg
MIR
AluJr4
L2
AluSc8
L3
U17
AluSg4
U1
L1MEd
7SLRNA
MER52A
MER11B
U2
L1M4c
U8
MER52D
MER58C
tRNA-Gly-GGA
U13
Tigger10
tRNA-Gly-GGG
MER101-int
SAR
tRNA-Ser-AGY
U14
Charlie14a
tRNA-Ala-GCY_
GSATX
MER57C1
tRNA-Leu-CTA
X8_LINE
tRNA-Ala-GCG
_GAATG_n
MER92A
GSAT
CR1-11_Crp
MLT1E1-int
tRNA-Ser-TCA_m_
CRP1
HERV1_LTRe
D)
Family
snoRNA
tRNA
centr
Satellite
Alu
snRNA
hAT-Tip100
ERVL
Gypsy
ERVK
ERV1
ERVL-MaLR
MIR
hAT-Blackjack
hAT-Charlie
L1
RTE-BovB
RTE-X
CR1
TcMar-Tigger
L2
RNA
TcMar-Mariner
srpRNA
-2
0
2
4
Multicopy gene family
Avg. log2 Fold Change
E) P301L vs WT sarkosyl insoluble gene type enrichment
P301L sarkosyl gene type enrichment (fold change)
WT sarkosyl gene type enrichment (fold change)
Mouse tau aggregate enrichment
4.5
4.0
3.5
3.0
2.5
2.0
1.5
1.0
0.5
0.0
0.0
0.5
1.0
1.5
2.0
2.5
3.0
3.5
TEC 1.431
transcribed_unprocessed_pseudogene 1.111
lncRNA 1.172
snRNA 2.071
rRNA 1.377
transcribed_unitary_pseudogene 0.786
unprocessed_pseudogene 0.802
Mt_rRNA 0.618
F) Mouse vs HEK293 gene type enrichment
20
10
5
2
1
0.5
0.2
0.1
0.05
0.02
0.01
0.2
0.5
1
2
5
10
20
snRNA
miRNA
Minor_snRNA
lncRNA
transcribed_processed_pseudogene
processed_pseudogene
snoRNA
polymorphic_pseudogene
protein_coding
TEC
ribozyme
misc_RNA
unprocessed_pseudogene
HEK293 tau aggregate enrichment
G) mRNAs significantly enriched in tau aggregates isolated from mouse brains
P301L enrichment score (Tau IP FPKM/Total RNA FPKM)
WT enrichment score (Tau IP FPKM/Total RNA FPKM)
8
7
6
5
4
3
2
1
0
1
2
3
4
5
6
7
Centrosomal mRNAs
Cep250
Cep164
Pcnt
Cep131
Splicing mRNAs
Prpf40b
Sart1
Snrnp70
Sart3
Clasrp
U2AF2
Red = 2X enriched in tau aggregates
Gray = Neither enriched nor depleted
Blue = 2X depleted from tau aggregates
H)
WT hTau
P301L hTau
Total
S1
P2
Total
S1
P2
Tau-12
Alpha-tubulin

Supplemental figure 2: Additional data on HEK293 and mouse brain tau aggregate isolation, related to figure 2. (A) Analysis of mRNAs two-fold enriched in tau aggregates from HEK293 cells (n = 2 biologic replicates). Genes with fewer than 5 FPKM were removed from analysis due to low coverage. Genes from the following groups were highlighted: Voltage-gated calcium channel proteins, histone proteins, centrosomal proteins, and splicing related proteins. **(B)** Cellular component gene ontology of the mRNAs that are two-fold enriched in tau aggregates. **(C, D)** Analysis of multicopy gene families using RepEnrich showing enrichment of specific snoRNA repeats (U8, U17, and U3; green), snRNA repeats (U1 and U2; red), tRNA species (blue), and Alu elements (orange). The gene family color scheme is shared between C and D. **(E)** Gene type enrichment in the P301L and WT sarkosyl insoluble samples. Fold change for each gene type was calculated by dividing the percentage of total FPKM made up by each gene type in the sarkosyl insoluble fraction (P2) by the percentage of total FPKM made up by each gene type in the total RNA. The numbers below the gene type names indicate the P301L/WT enrichment. Note the absence of snRNA enrichment in the sarkosyl insoluble fraction (n=2 biologic replicates). **(F)** Mouse vs HEK293 gene type enrichment. **(G)** Scatter plot of mRNA enrichment in mouse brain tau aggregates in P301L and WT mice. Enrichment scores were calculated by dividing the insoluble tau IP FPKM by the total RNA FPKM for each replicate. mRNAs in red are two-fold enriched and mRNAs in blue are two-fold depleted from the P301L sarkosyl insoluble tau IP. Genes with fewer than 5 FPKM were removed from analysis due to low coverage. Two groups of mRNAs were highlighted: centrosomal proteins and splicing related mRNAs. **(H)** Western blot of fractions from tau aggregate isolation showing P2 fraction (sarkosyl insoluble fraction) enriches for insoluble tau that is present in the P301L mice and not the WT mice.

Figure S3

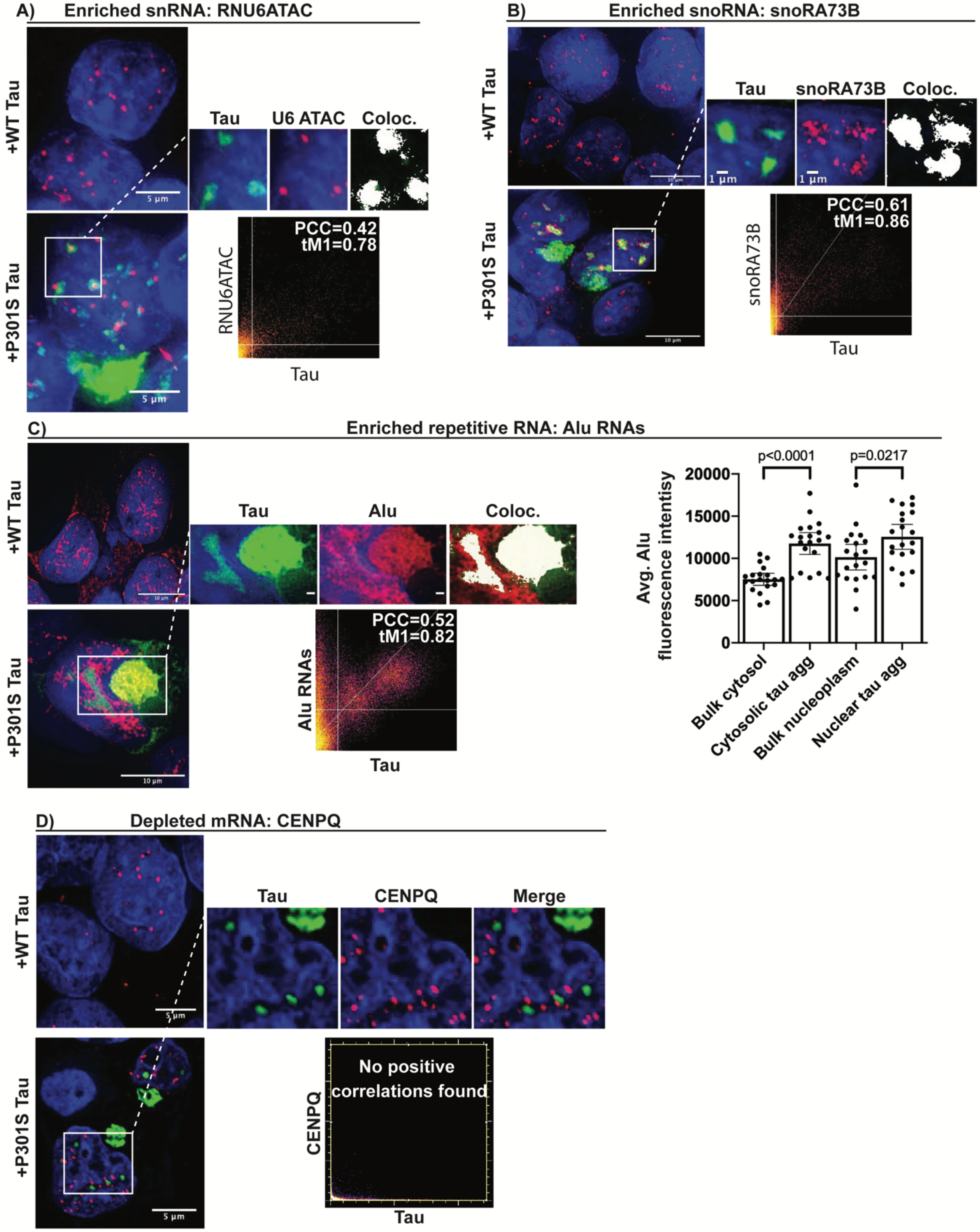

Supplemental figure 3: Additional FISH for RNAs in HEK293 tau biosensor cells, related to figure 3. (A, B) FISH of the enriched RNU6ATAC and snoRA73B shows overlapping fluorescence intensity in nuclear tau aggregates. **(C)** FISH for enriched multicopy Alu RNAs. Quantification shows enrichment in to nuclear and cytosolic tau aggregates, with greater enrichment into cytosolic tau aggregates relative to nuclear aggregates. Bar graphs show quantification of FISH fluorescence intensity within nuclear and cytosolic tau aggregates in relation to bulk cytosol and nucleoplasm. Data are represented as mean ± 95% confidence intervals and significance was determined using an unpaired two-tailed t-test (n=20 aggregates). White pixels in Coloc. images show pixels above the Costes determined thresholds in 2D intensity plots (PCC = Pearson correlation coefficient and tM1= thresholded manders colocalization (% of tau pixels above threshold that colocalize with Alu FISH pixels above threshold)). **(D)** FISH for the depleted mRNA, CENPQ, reveals lack of enrichment in nuclear and cytosolic tau aggregates.

Figure S4

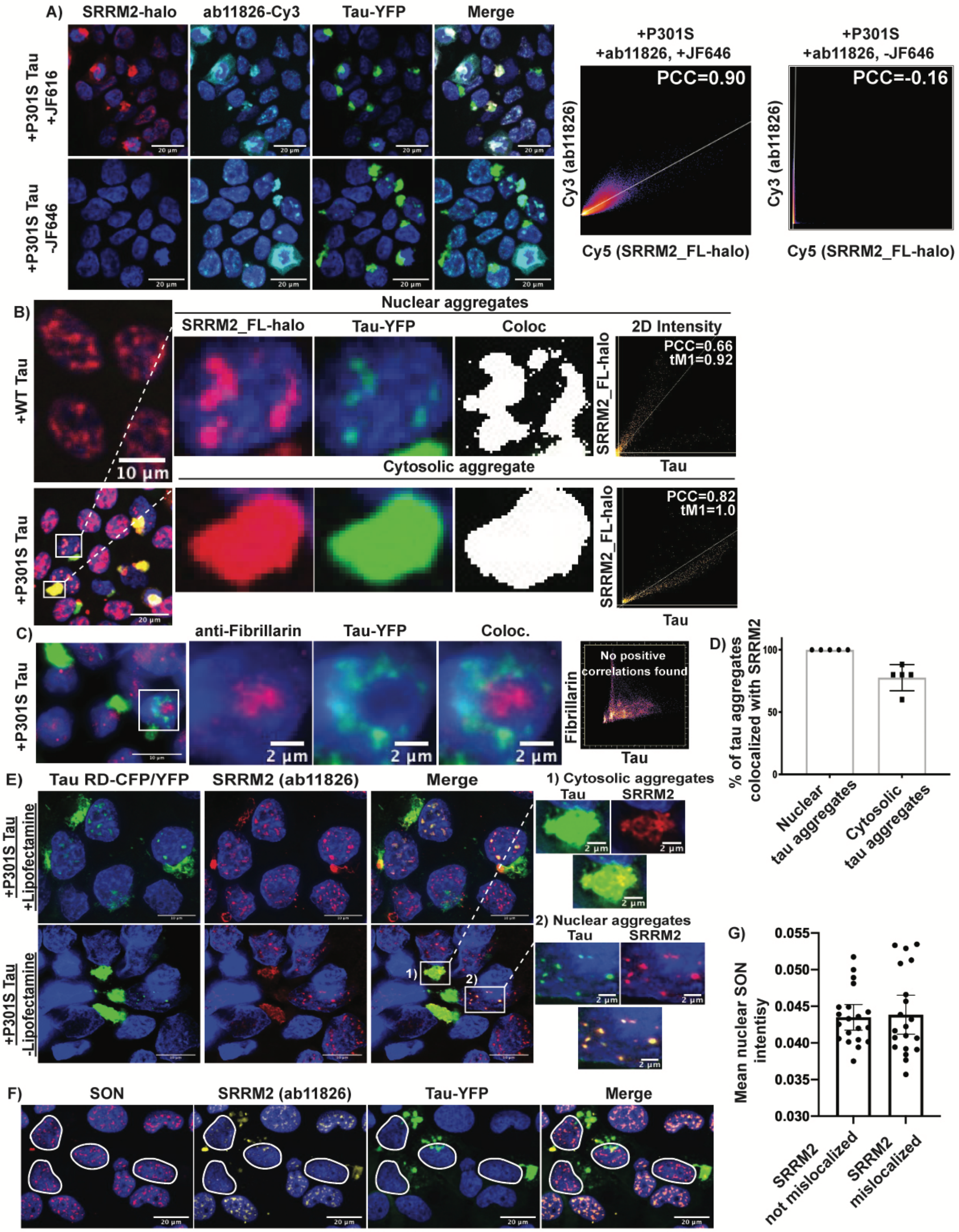
A)
SRRM2-halo
ab11826-Cy3
Tau-YFP
Merge
+P301S Tau +JF616
+P301S Tau -JF646
20 µm
+P301S +ab11826, +JF646
PCC=0.90
Cy3 (ab11826)
Cy5 (SRRM2_FL-halo)
+P301S +ab11826, -JF646
PCC=-0.16
Cy3 (ab11826)
Cy5 (SRRM2_FL-halo)
B)
+WT Tau
10 µm
Nuclear aggregates
SRRM2_FL-halo
Tau-YFP
Coloc
2D Intensity
PCC=0.66
tM1=0.92
SRRM2_FL-halo
Tau
+P301S Tau
Cytosolic aggregate
PCC=0.82
tM1=1.0
SRRM2_FL-halo
Tau
C)
+P301S Tau
anti-Fibrillarin
Tau-YFP
Coloc.
2 µm
No positive correlations found
Fibrillarin
Tau
D)
% of tau aggregates colocalized with SRRM2
100
50
0
Nuclear tau aggregates
Cytosolic tau aggregates
E)
Tau RD-CFP/YFP
SRRM2 (ab11826)
Merge
+P301S Tau +Lipofectamine
+P301S Tau -Lipofectamine
1) Cytosolic aggregates
Tau
SRRM2
2 µm
2) Nuclear aggregates
Tau
SRRM2
1)
2)
F)
SON
SRRM2 (ab11826)
Tau-YFP
Merge
20 µm
G)
Mean nuclear SON intentisy
0.055
0.050
0.045
0.040
0.035
0.030
SRRM2 not mislocalized
SRRM2 mislocalized

Supplemental figure 4: Additional HEK293 tau biosensor cell data, related to figure 4.
(A) Colocalization analysis of SRRM2_FL-halo and ab11826 in HEK293 cells showing pearson correlation coefficient of 0.90. To control for channel bleed, the same analysis was performed without addition of the JF646 halo ligand showing loss of colocalization and a decrease in the PCC to -0.16. **(B)** Images of HEK293 biosensor cells expressing SRRM2_FL-halo showing colocalization between nuclear and cytosolic tau aggregates. White pixels in Coloc. images show pixels above the Costes determined thresholds in 2D intensity plots (PCC = Pearson correlation coefficient and tM1= thresholded manders colocalization (% of tau pixels above threshold that colocalize with SRRM2_FL-halo pixels above threshold)). **(C)** IF for the nucleolar protein Fibrillarin showing lack of colocalization between tau aggregates and the nucleolus. Costes method was unable to identify a positive correlation to determine thresholds. **(D)** Analysis of the % of cytosolic tau aggregates that colocalize with SRRM2 in HEK293 tau biosensor cells. (n = 5 images, approximately 33 cells per image). Data are represented as mean ± 95% confidence interval. **(E)** Tau aggregates form in both the nucleus and the cytosol with and without lipofectamine 2000 as a transfection reagent. This shows lipofectamine is not necessary for SRRM2 mislocalization to cytosolic tau aggregates nor is it necessary for nuclear tau aggregate formation. **(F, G)** Analysis of whether SRRM2 mislocalization disrupts the formation of SON positive splicing speckles. Cells outlined in white are cells that have SRRM2 mislocalized to the cytosol. Quantification shows there is no significant change in average nuclear SON intensity with and without SRRM2 relocalization to cytoplasmic tau aggregates. Data are represented as mean ± 95% confidence intervals and significance was determined using an unpaired two-tailed t-test (n=20).

Figure S5

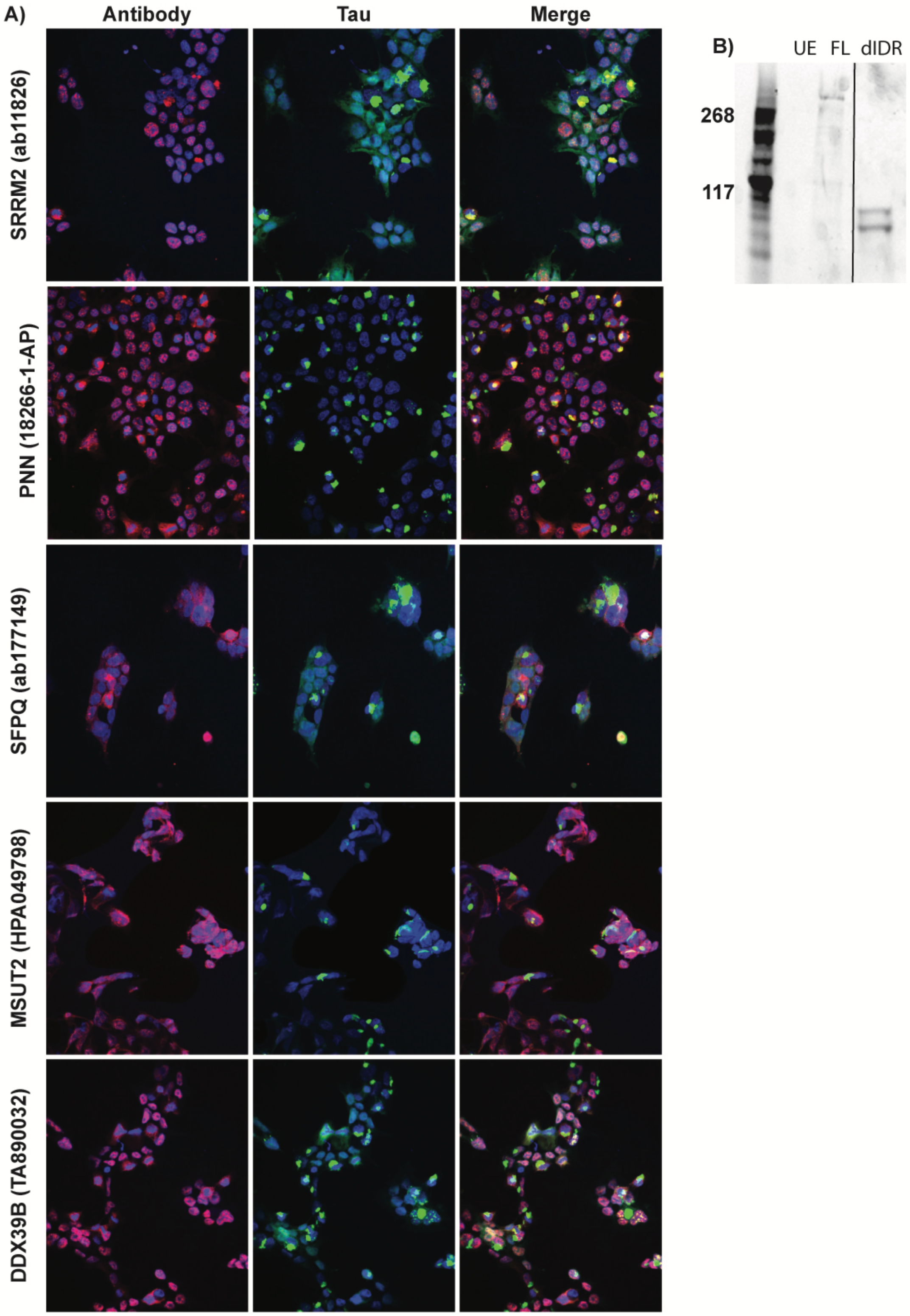
A)
Antibody
Tau
Merge
SRRM2 (ab11826)
PNN (18266-1-AP)
SFPQ (ab177149)
MSUT2 (HPA049798)
DDX39B (TA890032)
B)
UE
FL
dIDR
268
117

Supplemental Figure 5: Images of antibodies tested for enrichment in tau aggregates and truncation of SRRM2, related to figure 5. (A) Images of some of the proteins examined for their association with tau aggregates in Figs. 5 A, B. **(B)** Gel showing JF647 conjugated to halo fusion constructs (SRRM2_FL-halo and SRRM2_dIDR-halo) made using CRISPaint running at the appropriate sizes. All samples were run on the same gel, however the dIDR lane was not originally next to the FL lane and was placed next to it electronically for clarity. The cut is indicated with a black line.

Figure S6

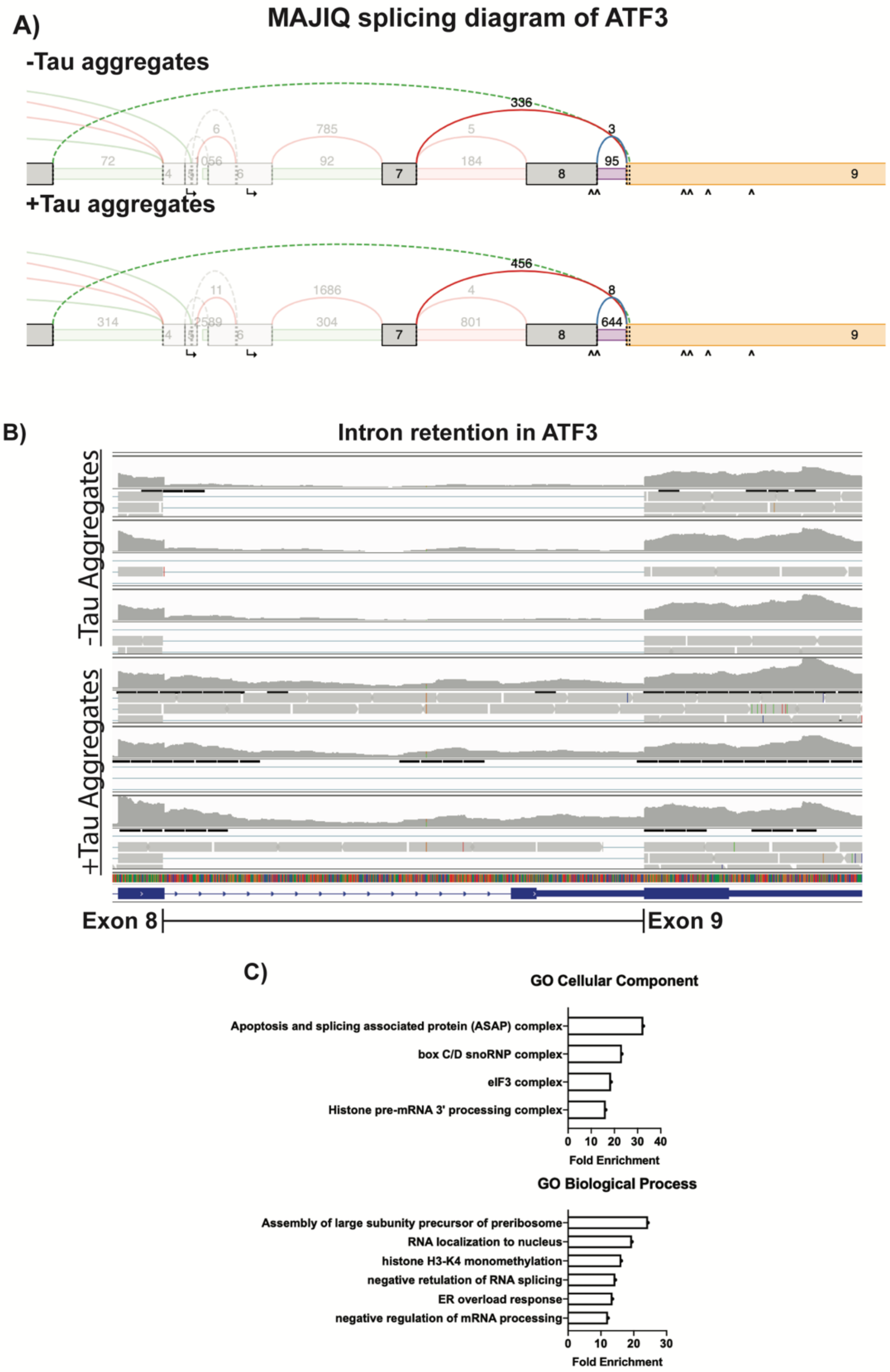
A)
MAJIQ splicing diagram of ATF3
-Tau aggregates
336
3
6
785
5
72
1056
92
184
95
4
7
8
9
+Tau aggregates
456
8
11
1686
4
314
2589
304
801
644
4
7
8
9
B)
Intron retention in ATF3
-Tau Aggregates
+Tau Aggregates
Exon 8
Exon 9
C)
GO Cellular Component
Apoptosis and splicing associated protein (ASAP) complex
box C/D snoRNP complex
eIF3 complex
Histone pre-mRNA 3' processing complex
0
10
20
30
40
Fold Enrichment
GO Biological Process
Assembly of large subunity precursor of preribosome
RNA localization to nucleus
histone H3-K4 monomethylation
negative retulation of RNA splicing
ER overload response
negative regulation of mRNA processing
0
10
20
30
Fold Enrichment

Supplemental Figure 6: Additional splicing analysis data from cells with and without tau aggregates, related to figure 6. (A) Example of intron retention between exon 8 and 9 in ATF3 identified by MAJIQ at ΔPSI threshold of 0.1 and confidence threshold of 0.95. The numbers above the splice sites are normalized read counts and show the increase in reads mapping to the intronic region between exons 8 and 9 (644 vs 95) in cells with tau aggregates. **(B)** Integrated genome viewer image showing raw read counts for each sequencing replicate. Intron retention can be seen between exon 8 and 9. **(C)** Gene ontology of the genes containing significantly retained introns in cells with tau aggregates (FDR < 0.05).

Figure S7

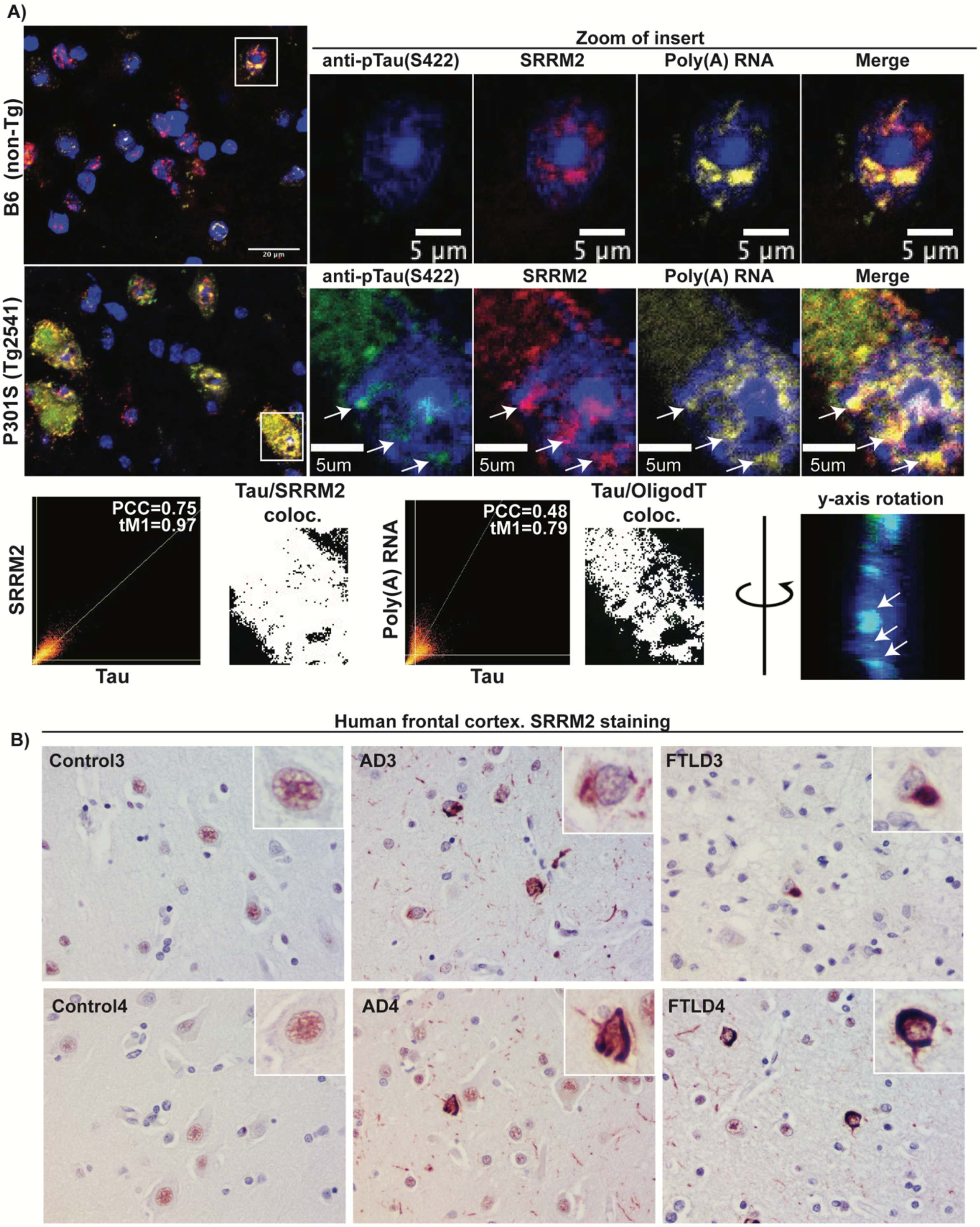

A)
B6 (non-Tg)
20 µm
Zoom of insert
anti-pTau(S422)
SRRM2
Poly(A) RNA
Merge
5 µm
P301S (Tg2541)
anti-pTau(S422)
SRRM2
Poly(A) RNA
Merge
5um
SRRM2
Tau
PCC=0.75
tM1=0.97
Tau/SRRM2 coloc.
Poly(A) RNA
Tau
PCC=0.48
tM1=0.79
Tau/OligodT coloc.
y-axis rotation
B)
Human frontal cortex. SRRM2 staining
Control3
AD3
FTLD3
Control4
AD4
FTLD4

Supplemental figure 7: Additional *in vivo* data from mouse and human tauopathies, related to figure 7. (A) IF and FISH showing p-tau (S422, ab79415) positive tau aggregates colocalized with SRRM2 (ab11826) and poly(A) RNA in the nucleus of Tg2541 mouse hindbrain. White pixels in coloc. images show pixels above the Costes determined thresholds in 2D intensity plots (PCC = Pearson correlation coefficient and tM1= thresholded manders colocalization (% of tau pixels above threshold that colocalize with red pixels above threshold)). Y-axis rotation shows that the pTau(S422) foci being interrogated in the zoomed images are within the nucleus rather than above or below the nucleus. **(B)** IHC in human brain showing cytosolic inclusions of SRRM2 (ab11826) in AD and FTLD patient brains, but not in control brains. (Patient information for this figure and figure 6B can be viewed in Table S3).